J. Math. Biol.
DOI 10.1007/s00285-014-0822-7

Mathematical Biology

Glioma follow white matter tracts: a multiscale DTI-based model

Christian Engwer · Thomas Hillen · Markus Knappitsch · Christina Surulescu

Received: 2 August 2013 / Revised: 28 July 2014

Abstract Gliomas are a class of rarely curable tumors arising from abnormal glia cells in the human brain. The understanding of glioma spreading patterns is essential for both radiological therapy as well as surgical treatment. Diffusion tensor imaging (DTI) allows to infer the white matter fibre structure of the brain in a noninvasive way. Painter and Hillen (J Theor Biol 323:25–39, 2013) used a kinetic partial differential equation to include DTI data into a class of anisotropic diffusion models for glioma spread. Here we extend this model to explicitly include adhesion mechanisms between glioma cells and the extracellular matrix components which are associated to white matter tracts. The mathematical modelling follows the multiscale approach proposed by Kelkel and Surulescu (Math Models Methods Appl Sci 23(3), 2012). We use scaling arguments to deduce a macroscopic advection-diffusion model for this process. The *tumor diffusion tensor* and the *tumor drift velocity* depend on both, the directions of the white matter tracts as well as the binding dynamics of the adhesion molecules. The advanced computational platform DUNE enables us to accurately solve our

C. Engwer · M. Knappitsch (✉)
Institut für Numerische und Angewandte Mathematik, WWU Münster, Münster, Germany
e-mail: markus.knappitsch@uni-muenster.de

C. Engwer
e-mail: christian.engwer@wwu.de

T. Hillen
Department of Mathematical and Statistical Sciences, Centre for Mathematical Biology, University of Alberta, Edmonton, AB, Canada
e-mail: thillen@ualberta.ca

C. Surulescu
Felix-Klein-Zentrum für Mathematik, Universität Kaiserslautern, Kaiserslautern, Germany
e-mail: surulescu@mathematik.uni-kl.de

Published online: 12 September 2014

macroscopic model. It turns out that the inclusion of cell binding dynamics on the microlevel is an important factor to explain finger-like spread of glioma.

Keywords Glioma modelling · Multiscale model · DTI data · Kinetic model

Mathematics Subject Classification 92C17 · 92C50 · 35Q92

1 Introduction

Gliomas are rarely curable brain tumors arising from abnormal glial cells in the human brain. Especially the most agressive type, *glioblastoma multiforme*, has a poor prognosis with a median survival rate that is <1 year (Wrensch et al. 2002). Complex therapy approaches including surgical resection of neoplastic tissue, radio- and chemo-therapy can still not ensure a complete healing of the patient and are part of ongoing research.

Modern methods such as *diffusion tensor imaging* are the preferred radiological diagnostic instruments (Sundgren et al. 2004). These techniques also allow revealing the specific architecture of a human brain in a noninvasive way. Particularly for surgical treatment of brain tumors this is valuable information. Detailed knowledge of the tissue structure can be used for modeling cellular movement in a mesoscopic framework (Hillen 2006; Painter and Hillen 2013). The respective settings involve kinetic transport equations, which provide an appropriate framework to account for patient specific diffusion tensor imaging (DTI) data and allow for modeling directly on the cell scale. Here we extend the results in Hillen and Painter (2013), Painter and Hillen (2013) to a multiscale framework also accommodating subcellular dynamics.

Starting from a mesoscopic transport equation for the cell density and under some appropriate assumptions we deduce an advection-diffusion equation for the tumor cell density via parabolic scaling. This corresponds to changing the time and space scales from minutes and micrometers (for cell movement) to weeks and centimeters (for glioma). The scaling will allow for characterizing the evolution of the macroscopic quantity of interest (i.e., cancer cell density) with the aid of an anisotropic *tumor diffusion tensor* and a *tumor drift velocity*. Their concrete forms follow from the underlying mesoscopic model, which renders this approach more precise than modeling directly on the macroscopic level. Using formal computations similar to those in the work of Painter and Hillen (2013) we show that the tumor diffusion tensor depends on the structure of the underlying fibre network, while the drift velocity contains two components, a directional one due to the underlying fibre network and a supplementary one, which is due to the binding of glioma to extracellular matrix (ECM) components that surrounds the fibre tracts. Our modeling approach is, however, more evolved, as it accounts for three spatiotemporal levels: the microscale for the subcellular dynamics, the mesoscale for migratory events on the cellular level, and the macroscale, on which the whole cell population, i.e. the tumor, is observed. Thus, we combine mathematical multiscale modeling with DTI data[1] and use numerical simulations in order to

[1] We obtained preprocessed DTI data by courtesy of Carsten Wolters and Felix Lucka, Institute for Biomagnetism und Biosignalanalysis, University of Münster. This includes segmentation data, the apparent water diffusion tensors as well as a brainmask for each voxel of the brain of a healthy male student.

forecast the anisotropic tumor spread. We find that our new model predicts finger-like invasion patterns for glioma, as observed in clinical practice, see e.g., Gerstner et al. (2010). Hence, we claim that these invasion patterns are more realistic than round-shaped predictions from isotropic diffusion models, but we have to leave a quantitative comparison with patient data to future research.

In Sects. 1.1 and 1.2 we provide a short review of biological and medical facts concerning neural structure, brain tumors and imaging techniques, followed by a description of cell movement by kinetic transport equations in Sect. 1.3. In Sect. 2.1, a (formal) deduction of the evolution equation for the macroscopic cell density is given, including the derivation of the tumor diffusion tensor and tumor drift velocity under involvement of DTI data. Numerical simulations for the macroscopic model are presented in Sect. 3, where we outline the potential benefit of this method. Finally, in Sect. 4 we discuss pros and cons of this modeling approach.

1.1 Brain anatomy and neurobiology of glioma growth

The human brain has a highly complex structure. Billions of neurons control the central nervous system and the peripheral nervous system, hence all our activities. It is estimated that a typical human brain consists of approximately 10^{11} neurons, each having a central part (soma), cellular extensions with many branches (dendrites), a long and thin element called *axon* and an axon terminal. Main components of the human brain are white matter, grey matter, blood, ECM, and cerebrospinal fluid (CSF). White matter is composed of glia cells and axonal nerve fibres. Since these are often myelinated, they are better visible due to their distinctive colour (Descoteaux 2008). Glia cells are another major component of human nervous tissue. They are responsible for the electric isolation of nerve cells and have a stabilizing function, acting as a support for these. There are several types of glia cells like astrocytes, oligodendrocytes, radial glia or Schwann cells.

Axons are often called *nerve fibres*, and bundles of myelinated axons are called *fibre tracts* (Descoteaux 2008). Diffusion along such fibre tracts differs significantly from diffusion happening orthogonally to them (Gritsenko et al. 2012). Modern imaging methods use this circumstance to reveal the human brain architecture by tracing the diffusion behaviour of injected water molecules (Hagman et al. 2006).

Neoplasms within the brain originate from the mutation of glia cells or neurons. They are difficult to treat and have a poor prognosis. Cancer cells are able to invade blood or lymph vessels, and subsequently circulate through the whole lymphatic and/or haemodynamic system (Geho et al. 2005). After extravasation, they continue growing and proliferating and build up secondary tumors. The most frequent types of brain tumors are gliomas (70 % incidence) and among them *glioblastoma multiforme* is the most malignant and frequent type (Ohgaki and Kleihues 2005).

The exact interaction of glioma cells with white matter tracts is largely unknown. What is known is that glioma do follow white matter tracts (D'Abaco and Kaye 2007; Giese and Kluwe 1996; Giese and Westphal 1996) and that several microbiological processes play in concert. Gritsenko et al. (2012) identified several ECM molecules which are highly expressed along myelinated fibres including hyaluronic acid (HA),

tenascin R, and leticans, which interconnect with each other and with the nerve fibres. The molecule HA is known to have a high water binding capacity, making the ECM softer compared to other areas in the brain. HA, tenascin and leticans bind to glioma cell surface receptors such as integrins, CD44 and ICAM-1. Integrins are transmembrane glycoproteins which are closely related to glioma invasion (Demuth and Berens 2004). The interaction of these molecules with several ECM components enable cells to adhere, to spread and to migrate, since they connect all interior components of the cell to the extracellular environment. As integrins are also responsible for the transduction of extracellular information into the cell interior, they influence cell growth, cell division, proliferation and apoptosis (Hood and Cheresh 2002; Huttenlocher and Horwitz 2011; Moschos et al. 2007).

For simplicity of our model in Sect. 2, we will refer to these receptors as "integrins", and the concentration of bound receptors is denoted with $y(t)$. Also we denote by $A(x, t)$ the generic ECM component. The mechanical details of the cell guidance along white matter tracts are unknown and it is believed that it results from a combination of reduced stiffness around nerve fibres, binding between ligands and ECM components and proteolytic activities. There are many more internal and external pathways at work, corresponding to the various processes which influence tumor migration. For example, *proteases* and MMPs degrade the ECM in a proteolytic process; cells might use chemotactic effects for directional guidance; cells interact with other glioma cells, with healthy cells and with the immune system. Here we focus only on the geometric aspects related to cell guidance and cell-ECM interactions, and we show that this effect is already able to explain finger-like spread of glioma.

1.2 Anisotropic diffusion: MRI, DTI and HARDI techniques

Since the random motility constant involved in the classical diffusion models does not carry any directional infomation, a tensor model which allows for capturing anisotropic aspects of diffusion has been poposed by Basser et al. (1992, 1993), Matiello and LeBihan (1994a, b). Thereby, the diffusion probability density function (pdf) of water is approximated by a tensor model, with a symmetric and positive definite tensor. The model is still Gaussian but it has six degrees of freedom instead of one. This idea led to *diffusion tensor imaging* (DTI). For more details about the physical background of the corresponding diffusion processes see e.g., Descoteaux (2008) and Tuch (1996).

As part of the diagnosis, modern imaging methods play a central role in the detection of brain tumors (Sundgren et al. 2004). Common high-resolution methods like computer tomography (CT) or especially magnetic resonace imaging (MRI) based methods like diffusion tensor imaging (DTI) (Hagman et al. 2006; LeBihan et al. 2001) or Q-ball imaging (QBI) (Descoteaux 2008; Tuch 1996, 2004) provide powerful noninvasive tools. The key idea of magnetic resonance imaging (MRI) relies on the diffusion behaviour of water molecules within structured tissue also containing information about the network architecture itself. Hence, these methods relate the anisotropy of water diffusion to the anisotropy of neural tissue, particularly of brain white matter (Hagman et al. 2006; Tuch 1996; Descoteaux 2008). The water molecules are assumed to spread in a Brownian way in an isotropic medium, thus there is no

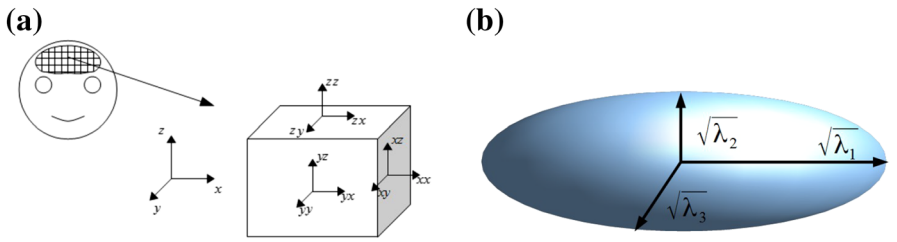

Fig. 1 Diffusion tensor imaging measures the spatial diffusion of water molecules by MRI per volume element. This yields a symmetric apparent water diffusion tensor which represents the directional dependent diffusivity of water molecules (**a**). Since there is no direct intuitive access to data in tensor form, ellipsoids can be used to vizualize data in tensor form. **b** The representation of the tensor by an ellipsoid, whose axes are scaled with the tensor eigenvalues $\lambda_1(\mathbf{x})$, $\lambda_2(\mathbf{x})$ and $\lambda_3(\mathbf{x})$. **a** Diffusion behaviour per volume element (voxel). **b** Representation of diffusion tensor data by an ellipsoid

directional preference. In contrast, in a fibrous or structured environment water molecules diffuse faster along the structure, which leads to anisotropy and also provides the physical basis for DTI. Despite this technological progress, the definitive diagnosis of the tumor can only be confirmed by histological examination of neoplastic tissue. This can be achieved e.g., by brain biopsy and is necessary for an optimal treatment strategy.

As mentioned, DTI measures the spatial diffusion of water molecules by MRI per volume element (voxel). This can be characterized with a symmetric diffusion tensor

$$\mathbb{D}_W(\mathbf{x}) = \begin{pmatrix} d_{xx}(\mathbf{x}) & d_{xy}(\mathbf{x}) & d_{xz}(\mathbf{x}) \\ d_{yx}(\mathbf{x}) & d_{yy}(\mathbf{x}) & d_{yz}(\mathbf{x}) \\ d_{zx}(\mathbf{x}) & d_{zy}(\mathbf{x}) & d_{zz}(\mathbf{x}) \end{pmatrix} \tag{1}$$

for each voxel, containing the full (apparent) diffusion information along six directions (see Fig. 1a). The orientation of fibre tracts within a voxel is of great interest. In this discrete, Cartesian view of the brain each voxel (**vo**lumetric pi**xel**) has a volume of $<1\,\mathrm{mm}^3$, hence a typical size of a DTI data set is of order 10^6. Thus, millions of tensors are needed to represent the tissue architecture of a human brain. Since we assumed that the diffusion is Gaussian, this approach is not capable to resolve multiple fibre crossings in a voxel and is therefore still not optimal. Recent improved high angular resolution imaging techniques [like e.g., HARDI (Descoteaux 2008; Tuch 2004; Descoteaux et al. 2009)] try to solve this problem.

In general, there are two main approaches to visualize a diffusion tensor, using either some scalar indices as *fractional anisotropy* (Beppu et al. 2003) or so called *tensor glyphs*. The latter encode the anisotropy structure of a tensor by a geometric object like *ellipsoids* or *peanuts* (Hagman et al. 2006). We discuss these two major approaches in more detail below. The fractional anisotropy is a scalar value between zero and one, calculated by using the eigenvalues of the apparent diffusion tensor. A value close to one means high anisotropy, i.e., a strong preference for a specific direction, whereas a very small value corresponds to the nearly isotropic case.

Since the diffusion tensor is assumed to be symmetric, it can be diagonalized. The obtained diagonal matrix features the eigenvalues $(\lambda_1(\mathbf{x}), \lambda_2(\mathbf{x}), \lambda_3(\mathbf{x}))$ on its main

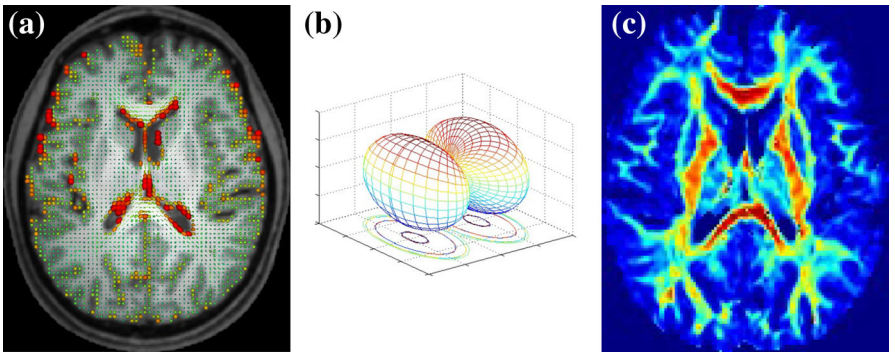

Fig. 2 Visualization of tensor data: ellipsoids, peanuts, and fractional anisotropy. **a** Representation of diffusion anisotropy by ellipsoids. **b** A peanut is given by the directional distribution function $\boldsymbol{\theta} \mapsto \boldsymbol{\theta}^t \mathbb{D}(\mathbf{x})\boldsymbol{\theta}$. **c** Fractional anisotropy index plotted for a horizontal slice of a human brain

diagonal. Then the *fractional anisotropy index* (FA) is defined per voxel (Hagman et al. 2006) by

$$FA(\mathbf{x}) = \frac{\sqrt{3}}{\sqrt{2}} \frac{\sqrt{(\lambda_1 - \overline{\lambda})^2 + (\lambda_2 - \overline{\lambda})^2 + (\lambda_3 - \overline{\lambda})^2}}{\sqrt{\lambda_1^2 + \lambda_2^2 + \lambda_3^2}} \tag{2}$$

with $\overline{\lambda} = \frac{\lambda_1+\lambda_2+\lambda_3}{3}$. A typical fractional anisotropy map is illustrated in Fig. 2c, where the FA-index is plotted for a horizontal slice of a human male brain. Observe that the FA index does not contain any directional information about the fibre tracts.

Tensor glyphs encode the information of a tensor in more detail than a scalar index does. Common glyphs are *ellipsoids* and *peanuts*. The diffusion ellipsoid is given by the 1-level set of $\boldsymbol{\theta}^t \mathbb{D}^{-1} \boldsymbol{\theta}$, which for a diagonal $\mathbb{D}$ takes the form

$$\frac{\theta_1^2}{\lambda_1} + \frac{\theta_2^2}{\lambda_2} + \frac{\theta_3^2}{\lambda_3} = 1.$$

If $(\lambda_i, \mathbf{v}_i)$ denotes the eigenvalue-eigenvector pairs of $\mathbb{D}$, then $\sqrt{\lambda_i}$ indicates the diffusivity in direction $\mathbf{v}_i$. In the case of isotropic tissue, for instance, where no direction is preferred by the diffusing water molecules, the corresponding ellipsoid is a ball. If the tissue is strictly aligned, there is one mean direction of diffusion, which is usually $\mathbf{v}_1$. Then the corresponding ellipsoid is cigar-shaped, see also Figs. 3a–i illustrating the connection between tissue architecture and diffusion ellipsoids.

As mentioned by Painter and Hillen (2013), instead of ellipsoids other objects having a *peanut*-like shape can also be used for the visualization (see Fig. 2b). These can be obtained when considering the *directional distribution function* q given by $\mathbb{S}^{n-1} \ni \boldsymbol{\theta} \mapsto \boldsymbol{\theta}^t \mathbb{D}(\mathbf{x})\boldsymbol{\theta} \in \mathbb{R}$. The corresponding object contains the same information as the ellipsoid. For each direction $\boldsymbol{\theta}$ given by a point on the unit-sphere $\mathbb{S}^{n-1}$ a peanut represents the diffusivity along that direction. Furthermore, the peanut is proportional to the mean squared displacement in direction $\boldsymbol{\theta}$, see Painter and Hillen (2013). We

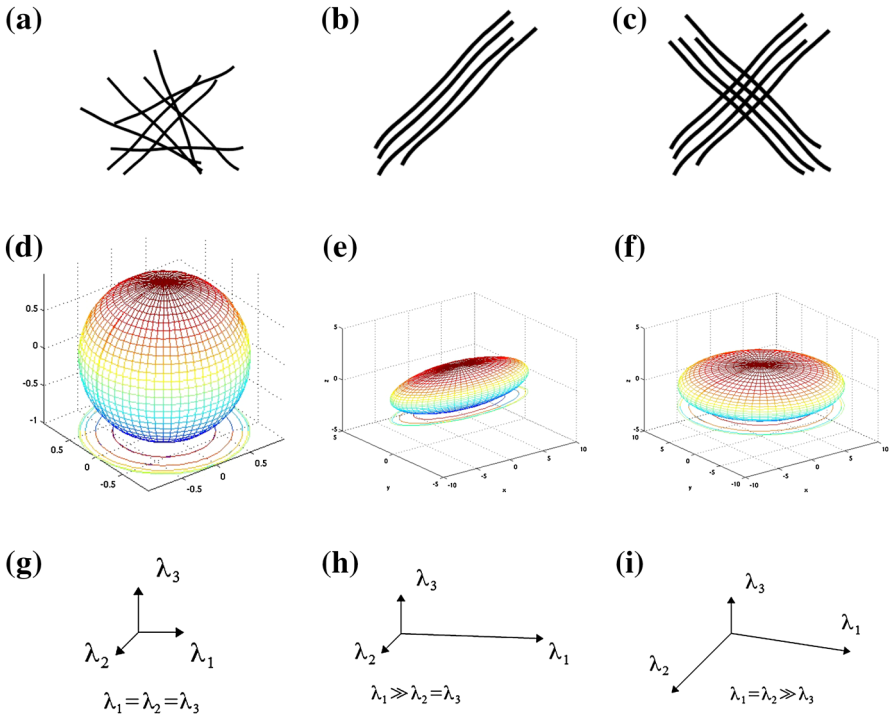

Fig. 3 Tissue architecture, tensor ellipsoids, and eigenvalues. **a** Isotropic case. Fibres are not aligned. **b** 1D alignment of fibres. Higher diffusivity in the alignment direction. **c** Two crossing fibre tracts: two main directions of diffusion. **d** Isotropic case: the diffusion ellipsoid is a ball. **e** Prolate diffusion: the diffusion ellipsoid is cigar-shaped for strictly aligned fibre tracts. **f** Oblate diffusion: the case with two crossing fibre tracts. **g** Isotropic case: all eigenvalues are of equal order, no directional preference. **h** One leading eigenvalue for one main direction of diffusion. **i** Crossing fibre tracts: two leading eigenvalues

will use a rescaled version of the peanut to define a directional distribution function based on tissue information obtained from DTI measurements.

1.3 Kinetic transport equations and cell movement

When observing systems of interacting biological entities, there are (at least) two major modeling approaches, according to whether the relevant dynamics are considered directly on the macroscopic population level or rather on the mesoscopic individual level. The first option provides a mean field view on a whole population. Thereby, on the one hand some information is lost about the individual behavior, but on the other hand the macroscopic setting offers a satisfactory overall description of the population. The second option allows for accommodating the individual behavior of the members in the population. The corresponding models are in general more complex than their macroscopic counterparts, but clearly ensure a more detailed description.

In the mesoscopic setting the dispersal and/or migration of cells is modelled by using kinetic transport equations featuring an integral operator for the characteriza-

tion of velocity innovations. This modeling framework was proposed by Alt (1980) and Othmer et al. (1988) in order to describe the motile behavior of organisms like bacteria under the influence of a chemotactic signal. Some rigorous results for a one-particle distribution function had already been provided by Stroock (1974) in a different context. More recently Hillen (2006) proposed a model for mesenchymal tumor invasion which is inspired by the setting in Alt (1980), Othmer et al. (1988) and which has been further developed for brain tumors (Painter and Hillen 2013) and for accounting for chemotaxis and cell–cell interactions (Chauviere et al. 2007). Ecological applications have been studied by Hillen and Painter (2013). A yet more general framework, the so-called kinetic theory of active particles (KTAP) was proposed by Bellomo et al. (2010).

Often it is possible to establish a connection between the mesoscopic and the macroscopic levels, e.g., by using some appropriate rescaling arguments and averaging, leading to evolution equations for the moments of the cell distribution function, see e.g., Filbet et al. (2005), Hillen (2006). For rigorous results on hyperbolic and parabolic limits of kinetic equations for chemotaxis we refer to (Chalub et al. 2004; Othmer and Hillen 2002; Hillen 2003). Further macroscopic models for cell migration directly rely on mass conservation and/or mechanical force balance (Anderson et al. 2000; Chaplain and Lolas 2006) or on the theory of mixtures (Barocas and Tranquillo 1997; Maini 1989; Tosin and Preziosi 2010; Traqui 1995).

During the last decades it has been recognized that the phenomena taking place on the macroscale are regulated by (and in turn influence) microscopic, subcellular processes in a sort of feedback mechanism. In particular, the binding of cell surface receptors like integrins to soluble and insoluble components of the ECM is seen as the onset of the subsequent intracellular signaling and its effects on the cell responses (e.g., polarization, proliferation, restructuring of the cytoskeleton etc.) (Hood and Cheresh 2002; Huttenlocher and Horwitz 2011). Multiscale models linking the subcellular with higher level (mesoscopic and/or macroscopic) descriptions offer a more detailed characterization of the migratory mechanism, but are also more difficult to handle. Among the first such models has been the one proposed by Firmani et al. (1999) for a tumor-immune system competition with medically induced activation-disactivation. The same idea was retaken later by Othmer et al. (Erban and Othmer 2005; Xue and Othmer 2009) and Bournaveas and Calvez (2008) in a multiscale description of bacterial chemotaxis, where the relevant intracellular signal transduction was modeled by an excitation-adaptation mechanism. A still related, but more detailed multiscale model for bacterial dispersal was provided by Surulescu and Surulescu (2010, 2011, 2013), where the authors also proposed an equation free model for the velocity jump movement of cells under the influence of a chemoattractant signal and of the intracellular dynamics. Numerical simulations for the macroscopic cell density have been performed via a nonparametric method, (see Surulescu and Surulescu (2010, 2011), to appear), an issue of particular importance, since no reliable numerical methods are available so far for handling a full multiscale setting connecting equations formulated on microscopic, mesoscopic, and macroscopic levels. This issue will be readressed later on in this work. Further descriptions—some of them even multiscale—of the interaction between tumor cells and the underlying tissue have been proposed, involving continuum mechanistic approaches (Chauviere and Preziosi 2010; Stolarska et al.

2009), discrete, or hybrid continuum-discrete settings (Chauviere et al. 2012; Frieboes et al. 2010; Hatzikirou and Deutsch 2008; Tanaka et al. 2009).

In the paper (Kelkel and Surulescu 2012) the authors started from the mesoscopic framework to deduce a multiscale model describing the evolution of tumor cell population density, whereby at the microscopic scale they did not account for genuine intracellular signaling, but rather for the above mentioned receptor dynamics on the cell surface. Transmembrane proteins called *integrins* provide linkages to the tissue fibres and to the ECM fragments resulting from proteolytic degradation. The latter acted as a chemoattractant, the evolution of which was characterized with a reaction-diffusion equation connected to the kinetic equation for the cell density and to the cell surface dynamics of integrins. In the paper (Kelkel and Surulescu 2011) the model also accounted for the dependence of proteolytic cutting on the fibre density in the direction of movement. Those concrete settings both align to the already mentioned KTAP theory proposed by Bellomo et al. (2010). Another class of multiscale models connecting the microscopic and macroscopic levels of cancer cell migration is considered e.g., in Meral and Surulescu (2013), Meral et al. (2013), Stinner et al. (2013), Szymanska et al. (2009), where the focus is on the effect of subcellular events on the tumor cell motility with more or less detailed description of the microscopic phenomena.

We consider here the mesoscopic (cell-level) setting obtained from describing the cell movement with the aid of velocity jump processes. The kinetic equation for the density function $p(t, \mathbf{x}, \mathbf{v}, \mathbf{y})$ of cells at time t, position $\mathbf{x} \in \mathbb{R}^n$, velocity $\mathbf{v} \in V \subset \mathbb{R}^n$, and internal state $\mathbf{y} \in Y \subset \mathbb{R}^p$ has the form, see e.g., Erban and Othmer (2005), Kelkel and Surulescu (2012),

$$\partial_t p + \nabla_{\mathbf{x}} \cdot (\mathbf{v} p) + \nabla_{\mathbf{y}} \cdot (\mathbf{G}(\mathbf{y}) p) = -\lambda(\mathbf{y}) p + \lambda(\mathbf{y}) \int_V K(\mathbf{x}, \mathbf{v}, \mathbf{v}') p(\mathbf{v}') d\mathbf{v}'. \quad (3)$$

Here $\mathcal{L}p := -\lambda(\mathbf{y}) p + \lambda(\mathbf{y}) \int_V K(\mathbf{x}, \mathbf{v}, \mathbf{v}') p(\mathbf{v}') d\mathbf{v}'$ is the *turning operator* modeling the cell velocity innovations due to contact guidance, environmental cues etc, and $\lambda(\mathbf{y})$ denotes the *turning rate* of cells.

The vector $\mathbf{y}$ stands for the internal state of a cell: its components can be e.g., concentrations of proteins involved in some intracellular signaling network or—as will be the case throughout this work—concentrations of adhesion molecules bound to soluble and/or unsoluble components of the cell environment. Its dynamics is characterized by a system of ordinary differential equations

$$\frac{d}{dt}\mathbf{y}(t) = \mathbf{G}(\mathbf{y}(t)), \quad (4)$$

where the right hand side is involving the concentrations/densities of the soluble/unsoluble environmental components as inputs.

The high dimensionality $(2n + p)$ of the state space renders the numerical handling of the multiscale model directly on the mesoscopic level very difficult. Also, we are not interested in computing the state and location of each individual cell on a timescale of seconds, but rather in the macroscopic spread of the glioma as a whole. Hence we employ parabolic scaling, to find a macroscopic model which describes the dynamics on macroscopic time and space scales. We will show later that the corresponding macroscopic model for the cell density

$$n(\mathbf{x}, t) := \int_Y \int_V p(t, \mathbf{x}, \mathbf{v}, \mathbf{y}) d\mathbf{v} d\mathbf{y}. \tag{5}$$

has the form of a *fully anisotropic advection-diffusion equation*

$$\partial_t n(\mathbf{x}, t) = \nabla\nabla : \left(\mathbb{D}_T(\mathbf{x}) n(\mathbf{x}, t)\right) + \nabla \cdot \left(\mathbf{u}(\mathbf{x}) n(\mathbf{x}, t)\right), \tag{6}$$

with a *tumor diffusion tensor* $\mathbb{D}_T(\mathbf{x})$ and a *tumor drift velocity* $\mathbf{u}(\mathbf{x})$. The operator $\nabla\nabla :$ is a short version of the full second order derivative

$$\nabla\nabla : (\mathbb{D}_T u) = \sum_{i,j=1}^{n} \frac{\partial}{\partial x_i} \frac{\partial}{\partial x_j} \left(D^{ij} u\right),$$

where D^{ij} denote the components of $\mathbb{D}_T$

Notice that (6) can equivalently be written in a more standard form as

$$\partial_t n(\mathbf{x}, t) = \nabla \cdot \left(\mathbb{D}_T(\mathbf{x}) \nabla n(\mathbf{x}, t)\right) + \nabla \cdot \left(\tilde{\mathbf{u}}(\mathbf{x}) n(\mathbf{x}, t)\right), \tag{7}$$

with $\tilde{\mathbf{u}} = \nabla \cdot \mathbb{D}_T + \mathbf{u}$. Since the diffusion tensor arises from the orientation of the tissue fibres, the term $\nabla \cdot \mathbb{D}_T$ appears as a *haptotaxis* term. Equation (7) provides a convenient split between diffusion and advection terms, which we will use later for our numerical simulations.

1.4 Previous models for glioma growth

Diffusion tensor imaging (DTI) data have been used previously in glioma modeling (Bondiau et al. 2008; Clatz et al. 2005; Cobzas et al. 2009; Jbabdi et al. 2005; Konukoglu et al. 2010; Mosayebi et al. 2010; Painter and Hillen 2013). Most of these models are set directly on the macroscopic level, using a scaled version of the DTI tensor as diffusion tensor for the tumor cells. The models have been compared to atlas data and to synthetic data, and they can be seen as an endorsement of the concept that anisotropic advection-diffusion equations are a promising framework for glioma spread. Our approach here supports this model class through our macroscopic scaling analysis. We are able to derive the diffusion tensor and the drift velocity from biologically reasonable assumptions.

Our model differs from the previous kinetic setting in the reference (Painter and Hillen 2013) by the inclusion of a supplementary scale, in order to account for the cell-ECM interactions on the microscopic level, as proposed by Kelkel and Surulescu (2011, 2012) in a more general framework. Our simulations show that these interactions play an important role in the glioma spread patterns.

2 The mesoscopic and macroscopic models

2.1 Cell-ECM interactions

As mentioned before, in this work we aim for a multiscale description of glioma invasion. Starting from the receptor dynamics on the cell surface at the microscale level, we progress to the higher mesoscopic level to a kinetic transport equation. From this an evolution equation for the macroscopic cell density will be deduced with the aid of a parabolic scaling. Since our focus is here on the interaction between tumor cells and tissue and their effects on glioma invasion we do not account for chemotactic effects on the migratory behavior, nor for the proteolytic degradation of tissue fibres. Our model is built on the framework proposed by Kelkel and Surulescu (2011, 2012), in which additionally the fibre residuals resulting by the action of matrix degrading enzymes were playing the role of a chemoattractant for the moving cells. Hence, the present model is a simplified version of the more general setting in the papers by Kelkel and Surulescu (2011, 2012).

For the microscopic dynamics we make the following assumptions:

1. The free receptors (e.g. integrins) on the cell surface bind to the underlying ECM. This process is described on the microscale by an ordinary differential equation for the density of bound receptors $y(t)$, leading to an additional transport term in our model on the mesoscopic level. We assume that binding occurs preferentially in areas of highly aligned tissue.
2. The turning rate of the cells depends on the receptor state on the cell surface. We assume that if many receptors are occupied,then it is expected to increase, since in that case the cell will need to change its direction more often in order to 'free' itself from the too densely packed fibres surrounding it (Sun et al. 2006).
3. The turning behaviour of the cells can be described by a *turning kernel* dictating the choice of the new moving direction upon conditioning on the previous velocity regime and/or the integrin dynamics.
4. Let us denote by $A(t, \mathbf{x})$ the volume fraction of the ECM components which are expressed in between myelinated brain fibres (HA, tenascin, leticans). Since the fractional anisotropy is a measure for the alignment for the brain fibres, we assume that the ECM components are proportional to the fractional anisotropy of the fibres, i.e. $A(x, t) = \mathrm{FA}(x, t)$.

Starting from simple mass action kinetics, the receptor dynamics on the cell surface is described by the following ordinary differential equation:

$$\dot{y} = k^+(R_0 - y)A - k^- y,$$

where R_0 denotes the total number of receptors on the cell (we assume it is conserved), whereas $y(t)$ gives the density of receptors bound to ECM. The constants k^+ and k^- denote the reaction rates for the reversible binding of adhesion molecules to the tissue fibres. Note that since A is not a classical density measured in M = mol/l, the k^+ constant is not the classical association rate for second order reactions with unit $\mathrm{M}^{-1}\mathrm{s}^{-1}$ (Lauffenburger and Lindermann 1993), but is a measure for how many

receptors of a cell with R_0 receptors are bound per unit time. Hence, both k^+ and k^- have unit s^{-1}. The subsequent analysis follows the idea of Erban and Othmer (2005).

The steady state of this equation is $y^* = \frac{k^+ A R_0}{k^+ A + k^-}$. Further, let us introduce a new internal variable $z := y^* - y$ measuring deviations from the steady state. Next consider the path of a single cell starting in $\mathbf{x}_0$ and moving with velocity $\mathbf{v}$ through a time-invariant density field $A(\mathbf{x})$. Then with the notations $\mathbf{x} = \mathbf{x}_0 + \mathbf{v}t$ and

$$f(A(\mathbf{x})) = \frac{k^+ A(\mathbf{x}) R_0}{k^+ A(\mathbf{x}) + k^-} \tag{8}$$

it follows that for any t

$$\frac{d}{dt} f\big(A(\mathbf{x}_0 + \mathbf{v}t)\big) = f'(A(\mathbf{x}_0 + \mathbf{v}t))\ \mathbf{v} \cdot \nabla A(\mathbf{x}_0 + \mathbf{v}t)$$

and hence z satisfies the equation

$$\begin{aligned} \dot{z} &= -(k^+ A(\mathbf{x}) + k^-) z + f'(A(\mathbf{x})) \mathbf{v} \cdot \nabla A(\mathbf{x}) \\ &= -(k^+ A(\mathbf{x}) + k^-) z + \frac{k^+ k^- R_0}{(k^+ A(\mathbf{x}) + k^-)^2}\ \mathbf{v} \cdot \nabla A(\mathbf{x}). \end{aligned} \tag{9}$$

This equation can be solved explicitly for z to yield

$$z(t) = (y^* - y_0) e^{-(k^+ A + k^-)t} + (1 - e^{-(k^+ A + k^-)t}) \frac{k^+ k^- R_0}{(k^+ A + k^-)^3}\ \mathbf{v} \cdot \nabla A,$$

where $y_0 = y(0)$. Hence, z is bounded as long as ∇A is and its sign depends on the current orientation of the cell w.r.t. the gradient of the fibre volume fraction.

For the turning rate we choose

$$\lambda(z) = \lambda_0 - \lambda_1 z \geq 0, \tag{10}$$

where λ_0 and λ_1 are some positive constants. Note that this is equivalent to considering $\lambda(y) = \lambda_0 - \lambda_1 y^* + \lambda_1 y$, which becomes indeed larger when many receptors are bound to the tissue. This choice corresponds to the one proposed by Erban and Othmer (2005) for the turning rate of bacteria and—after a linearization—also to that chosen by Grünbaum (2000).

2.2 The corresponding transport equation

With the above model for the internal dynamics equation (3) reads

$$\begin{aligned} &\partial_t p + \nabla_{\mathbf{x}} \cdot (\mathbf{v} p) + \partial_z \left(\left(-(k^+ A + k^-) z + f'(A(\mathbf{x}))\ \mathbf{v} \cdot \nabla A \right) p \right) \\ &\quad = -\lambda(z) p + \lambda(z) \int_V K(\mathbf{x}, \mathbf{v}, \mathbf{v}') p(\mathbf{v}') d\mathbf{v}'. \end{aligned} \tag{11}$$

We now focus on the case where the cell speed is constant s, hence we have $V = s\mathbb{S}^{n-1}$. Furthermore, we choose $K(\mathbf{x}, \mathbf{v}, \mathbf{v}') = \frac{q(\hat{\mathbf{v}})}{\omega}$ with $\omega = \int_V q(\hat{\mathbf{v}})d\mathbf{v} = s^{n-1}$ a scaling constant, as proposed by Hillen (2005) and Painter and Hillen (2013) according to our assumption that cells choose new directions of movement due to contact guidance. Recall that q denotes the directional distribution of tissue fibres, thus we also assume the tissue to be undirected. Additionally, we choose a linear turning rate $\lambda(z) = \lambda_0 - \lambda_1 z$, and have hence the transport equation

$$\begin{aligned} &\partial_t p + \nabla_{\mathbf{x}} \cdot (\mathbf{v}p) - \partial_z \left(\left((k^+ A + k^-)z - f'(A(\mathbf{x}))\, \mathbf{v} \cdot \nabla A \right) p \right) \\ &\quad = -\lambda_0 p + \lambda_1 z p + \lambda_0 \frac{q}{\omega} \int_V p(\mathbf{v}')d\mathbf{v}' - \lambda_1 \frac{q}{\omega} \int_V z p(\mathbf{v}')d\mathbf{v}'. \end{aligned} \tag{12}$$

Next introduce the following moments:

$$\begin{aligned} m(t, \mathbf{x}, \mathbf{v}) &= \int_Z p(t, \mathbf{x}, \mathbf{v}, z)dz, & M(t, \mathbf{x}) &= \int_V \int_Z p(t, \mathbf{x}, \mathbf{v}, z)dzd\mathbf{v} \\ m^z(t, \mathbf{x}, \mathbf{v}) &= \int_Z z p(t, \mathbf{x}, \mathbf{v}, z)dz, & M^z(t, \mathbf{x}) &= \int_V \int_Z z p(t, \mathbf{x}, \mathbf{v}, z)dzd\mathbf{v}, \end{aligned}$$

where our new domain for the internal dynamics is $Z \subseteq [y^* - R_0, y^*]$. In the following we assume the data to be compactly supported in the $(\mathbf{x}, \mathbf{v}, z)$-space, which allows to perform the subsequent calculations.

Integrate (12) with respect to z:

$$\partial_t m + \mathbf{v} \cdot \nabla m = -\lambda_0 m + \lambda_1 m^z + \lambda_0 \frac{q}{\omega} M - \lambda_1 \frac{q}{\omega} M^z. \tag{13}$$

Multiply (12) by z and integrate again:

$$\begin{aligned} &\partial_t m^z + \mathbf{v} \cdot \nabla m^z - \int_Z z \cdot \left[\partial_z \left(\left[(k^+ A + k^-)z - f'(A(\mathbf{x}))\, \mathbf{v} \cdot \nabla A \right] p \right) \right] dz \\ &\quad = -\lambda_0 m^z + \lambda_1 m^{zz} + \lambda_0 \frac{q}{\omega} M^z - \lambda_1 \frac{q}{\omega} M^{zz} \end{aligned}$$

with

$$m^{zz}(t, \mathbf{x}, \mathbf{v}) = \int_Z z^2 p(t, \mathbf{x}, \mathbf{v}, z)dz \text{ and } M^{zz}(\mathbf{x}, t) = \int_V \int_Z z^2 p(t, \mathbf{x}, \mathbf{v}, z)dzd\mathbf{v}.$$

Assume the internal dynamics equilibrates rapidly, so that the system is always close to the steady state. Hence, we neglect the second-order moments in z, so that the last equation becomes

$$\partial_t m^z + \mathbf{v} \cdot \nabla m^z = -(k^+ A + k^-)m^z + f'(A(\mathbf{x}))\, \mathbf{v} \cdot \nabla A\, m - \lambda_0 m^z + \lambda_0 \frac{q}{\omega} M^z.$$

2.3 Parabolic scaling

Now, use a parabolic scaling: $\hat{t} = \varepsilon^2 t,\ \hat{\mathbf{x}} = \varepsilon \mathbf{x}$, then drop the hats on $\mathbf{x},\ t$. This yields two equations:

$$\varepsilon^2 \partial_t m + \varepsilon \mathbf{v} \cdot \nabla m = -\lambda_0 m + \lambda_1 m^z + \lambda_0 \frac{q}{\omega} M - \lambda_1 \frac{q}{\omega} M^z \tag{14}$$

$$\varepsilon^2 \partial_t m^z + \varepsilon \mathbf{v} \cdot \nabla m^z = -(k^+ A + k^-) m^z + \varepsilon f'(A(\mathbf{x}))\ \mathbf{v} \cdot \nabla A\ m - \lambda_0 m^z + \lambda_0 \frac{q}{\omega} M^z. \tag{15}$$

Next, use Hilbert expansions for m, M, m^z and M^z:

$$\begin{aligned} m &= m_0 + \varepsilon m_1 + \varepsilon^2 m_2 + \dots \\ M &= M_0 + \varepsilon M_1 + \varepsilon^2 M_2 + \dots \\ m^z &= m_0^z + \varepsilon m_1^z + \varepsilon^2 m_2^z + \dots \\ M^z &= M_0^z + \varepsilon M_1^z + \varepsilon^2 M_2^z + \dots \end{aligned}$$

and collect terms of equal order in ε:

ε^0:

$$0 = -\lambda_0 m_0 + \lambda_1 m_0^z + \lambda_0 \frac{q}{\omega} M_0 - \lambda_1 \frac{q}{\omega} M_0^z \tag{16}$$

$$0 = -(k^+ A + k^-) m_0^z - \lambda_0 m_0^z + \lambda_0 \frac{q}{\omega} M_0^z. \tag{17}$$

ε^1:

$$\mathbf{v} \cdot \nabla m_0 = -\lambda_0 m_1 + \lambda_1 m_1^z + \lambda_0 \frac{q}{\omega} M_1 - \lambda_1 \frac{q}{\omega} M_1^z \tag{18}$$

$$\mathbf{v} \cdot \nabla m_0^z = -(k^+ A + k^-) m_1^z + f'(A(\mathbf{x}))\ \mathbf{v} \cdot \nabla A\ m_0 - \lambda_0 m_1^z + \lambda_0 \frac{q}{\omega} M_1^z. \tag{19}$$

ε^2:

$$\partial_t m_0 + \mathbf{v} \cdot \nabla m_1 = -\lambda_0 m_2 + \lambda_1 m_2^z + \lambda_0 \frac{q}{\omega} M_2 - \lambda_1 \frac{q}{\omega} M_2^z. \tag{20}$$

By integrating with respect to $\mathbf{v}$ it follows from (16) to (20):

ε^0:

$$\begin{aligned} &\text{From eq. (17)}: \quad M_0^z = 0,\ m_0^z = 0. \\ &\text{From eq. (16)}: \quad m_0 = \frac{q}{\omega} M_0. \end{aligned}$$

ε^1 (recall the assumption of undirected tissue):

$$\text{From eq. (19)}: \quad M_1^z = 0, m_1^z = (k^+ A + k^- + \lambda_0)^{-1}\ m_0\ f'(A(\mathbf{x}))\ \mathbf{v} \cdot \nabla A(\mathbf{x})$$

$$\text{From eq. (18)}: \quad M_1 = 0,\ m_1 = -\frac{1}{\lambda_0}\left(\mathbf{v}\cdot\nabla m_0 - \lambda_1 m_1^z\right).$$

Indeed, we use the properties of the operator $\mathcal{L}[\lambda_0](m_1) := -\lambda_0 m_1 + \lambda_0 \frac{q}{\omega} M_1$ defined on $L^2_q(V)$. The latter is a weighted L^2-space, with weight function $q^{-1}(\hat{\mathbf{v}})$. For the kernel of $\mathcal{L}[\lambda_0]$ we have

$$\mathcal{L}[\lambda_0](m_1) = 0 \qquad \Longleftrightarrow \qquad m_1 = \frac{\hat{q}(\hat{\mathbf{v}})}{\omega} M_1.$$

The mapping $\mathcal{L}[\lambda_0]$ is a compact Hilbert-Schmidt operator (see Hillen and Othmer 2000) whose kernel is given by the linear space $\langle q\rangle$, denoting the subspace of $L^2_q(V)$ spanned by q.
Then (see again Hillen and Othmer 2000) on $\langle q\rangle^\perp$ we can find the pseudo-inverse of $\mathcal{L}[\lambda_0]$. Consider for this a given function $\psi \in \langle q\rangle^\perp$ and solve

$$\mathcal{L}[\lambda_0](m_1) = \psi.$$

Since $m_1 \in \langle q\rangle^\perp$ we have $M_1 = 0$ and the rest follows immediately.

Now, we can collect known expressions and write them w.r.t. M_0.

$$\begin{aligned}
m_0 &= \frac{q}{\omega} M_0 \\
m_1^z &= \left(k^+ A + k^- + \lambda_0\right)^{-1} f'(A(\mathbf{x}))\ \mathbf{v}\cdot\nabla A \frac{q}{\omega} M_0 \\
m_1 &= -\frac{1}{\lambda_0}\left[\mathbf{v}\cdot\nabla\left(\frac{q}{\omega}M_0\right) - \lambda_1\left(k^+A + k^- + \lambda_0\right)^{-1} f'(A(\mathbf{x}))\ \mathbf{v}\cdot\nabla A\frac{q}{\omega}M_0\right].
\end{aligned}$$

Integration of (20) w.r.t. $\mathbf{v}$ yields

$$\int_V \left(\partial_t \frac{q}{\omega} M_0 + \mathbf{v}\cdot\nabla m_1\right) d\mathbf{v} = 0.$$

With the terms calculated above and a function $g(A)$ representing the influence of the receptor dynamics given by

$$g(A(\mathbf{x})) = \lambda_1 (k^+ A(\mathbf{x}) + k^- + \lambda_0)^{-1} f'(A(\mathbf{x})),$$

this gives

$$\partial_t M_0 + \int_V \mathbf{v}\cdot\nabla\left[-\frac{1}{\lambda_0}\left(\mathbf{v}\cdot\nabla\left(\frac{q}{\omega}M_0\right) - g(A(\mathbf{x}))\ \mathbf{v}\cdot\nabla A\frac{q}{\omega}M_0\right)\right] d\mathbf{v} = 0,$$

which is equivalent to

$$\begin{aligned}
\partial_t M_0 &- \frac{1}{\lambda_0}\int_V \mathbf{v}\cdot\nabla\left(\mathbf{v}\cdot\nabla\left(\frac{q}{\omega}M_0\right)\right) d\mathbf{v} \\
&+ \frac{1}{\lambda_0}\int_V \mathbf{v}\cdot\nabla\left(g(A(\mathbf{x}))\ \mathbf{v}\cdot\nabla A\ \frac{q}{\omega}M_0\right) d\mathbf{v} = 0.
\end{aligned}$$

We end up with an evolution equation for M_0, given by

$$\partial_t M_0 - \frac{1}{\lambda_0}\nabla\cdot\left(\int_V \mathbf{v}\otimes\mathbf{v}\nabla\frac{q}{\omega}d\mathbf{v}\; M_0\right) - \frac{1}{\lambda_0}\nabla\cdot\left(\int_V \mathbf{v}\otimes\mathbf{v}\frac{q}{\omega}d\mathbf{v}\,\nabla M_0\right) + \frac{1}{\lambda_0}\int_V \mathbf{v}\cdot\nabla\left(g(A(\mathbf{x}))\,\mathbf{v}\cdot\nabla A\,\frac{q}{\omega}\,M_0\right)d\mathbf{v} = 0.$$

This leads to the evolution equation

$$\partial_t M_0 - \nabla\cdot(\mathbb{D}_T(\mathbf{x})\nabla M_0) + \nabla\cdot([g(A(\mathbf{x}))\mathbb{D}_T(\mathbf{x})\nabla A(\mathbf{x}) - \mathbf{u}(\mathbf{x})]\,M_0) = 0 \quad (21)$$

with the tumor diffusion tensor

$$\mathbb{D}_T(\mathbf{x}) = \frac{1}{\lambda_0\omega}\int_V \mathbf{v}\otimes\mathbf{v}q\,d\mathbf{v},$$

and a tumor drift velocity which can be written as

$$\mathbf{u}(\mathbf{x}) = \frac{1}{\lambda_0\omega}\int_V \mathbf{v}\otimes\mathbf{v}\nabla q\,d\mathbf{v}.$$

Remark 1
- Notice the suplementary term (in comparison to the macroscopic equations, e.g., in the paper by Hillen (2006) involving the gradient of the fibre volume fraction. It highlights the haptotactic character of cell movement influenced by the receptor binding dynamics on the cell surface.
- Equation (21) can also be rewritten in the fully anisotropic form

$$\partial_t M_0 - \nabla\nabla : (\mathbb{D}_T(\mathbf{x})\;M_0) + \nabla\cdot(g(A(\mathbf{x}))\mathbb{D}_T(\mathbf{x})\nabla A(\mathbf{x})M_0) = 0.$$

2.4 Determination of the coefficients

In order to determine an explicit form for the coefficients $\mathbb{D}_T(\mathbf{x})$, and $\mathbf{u}(\mathbf{x})$ we need to characterize the fibre distribution $q(\mathbf{x},\boldsymbol{\theta})$. As already mentioned, the aim is to embed DTI data into our model equations. Thereby, a possible choice can be (Hillen and Painter 2013; Painter and Hillen 2013)

$$q(\mathbf{x},\boldsymbol{\theta}) = \frac{n}{|\mathbb{S}^{n-1}|\mathrm{tr}\mathbb{D}_W(\mathbf{x})}\boldsymbol{\theta}^t\mathbb{D}_W(\mathbf{x})\boldsymbol{\theta}. \quad (22)$$

The *water diffusion tensor* $\mathbb{D}_W(\mathbf{x})$ can be obtained for each voxel $\mathbf{x}$ by measurements, hence the above formula allows for computing the fibre distribution function for each voxel.

Remark 2 Painter and Hillen (2013) argued that this choice for the relationship between fibre orientation and water diffusion data encompasses some significant shortcomings. Hence, instead of (22), a bimodal von Mises-Fisher distribution (see e.g.,

Mardia and Jupp 1999) of the form

$$q(\mathbf{x},\boldsymbol{\theta}) = \frac{k(\mathbf{x})}{8\pi\,\sinh(k(\mathbf{x}))}\left(e^{k\boldsymbol{\phi}\cdot\boldsymbol{\theta}} + e^{-k\boldsymbol{\phi}\cdot\boldsymbol{\theta}}\right) \tag{23}$$

has been chosen, with $k(\mathbf{x}) = \kappa \cdot \mathrm{FA}(\mathbf{x})$, where $\mathrm{FA}(\mathbf{x})$ denotes the fractional anisotropy and $\boldsymbol{\phi}$ represents the leading eigenvector of the diffusion tensor for each voxel. In this approach, the concentration parameter κ has to be determined[2] and it can be interpreted as the sensitivity of the cells to the orientation of the underlying fibre structure.

In order to avoid introducing more parameters for which the identification is still unclear in practice, we will keep the form (22) for q. However, in Sect. 3 we will also consider the alternative fibre distribution (23) and compare the results obtained for both choices.

Now (see also Painter and Hillen 2013) the tumor diffusion tensor has the following structure:

$$\mathbb{D}_T(\mathbf{x}) = \frac{s^2}{\lambda_0(n+2)}\left(\mathbb{I}_n + 2\frac{\mathbb{D}_W(\mathbf{x})}{\mathrm{tr}\mathbb{D}_W(\mathbf{x})}\right). \tag{24}$$

From this and our choice of the fibre distribution q we can compute (upon using the notation $\omega_n = |\mathbb{S}^{n-1}|$):

$$\mathbf{u}(\mathbf{x}) = \frac{s^{n+1}}{\lambda_0\omega}\frac{n}{\omega_n}\int_{\mathbb{S}^{n-1}} \boldsymbol{\theta}\boldsymbol{\theta}^t \nabla\left(\frac{1}{\mathrm{tr}\mathbb{D}_W(\mathbf{x})}\boldsymbol{\theta}^t\mathbb{D}_W(\mathbf{x})\boldsymbol{\theta}\right) d\boldsymbol{\theta}.$$

First, we have

$$\begin{aligned}
&\nabla_{\mathbf{x}}\left(\frac{1}{\mathrm{tr}\mathbb{D}_W(\mathbf{x})}\boldsymbol{\theta}^t\mathbb{D}_W(\mathbf{x})\boldsymbol{\theta}\right)\\
&= \nabla_{\mathbf{x}}\left(\frac{1}{\mathrm{tr}\mathbb{D}_W(\mathbf{x})}\right)\boldsymbol{\theta}^t\mathbb{D}_W(\mathbf{x})\boldsymbol{\theta} + \frac{1}{\mathrm{tr}\mathbb{D}_W(\mathbf{x})}\nabla_{\mathbf{x}}\left(\boldsymbol{\theta}^t\mathbb{D}_W(\mathbf{x})\boldsymbol{\theta}\right)\\
&= -\nabla_{\mathbf{x}}(\mathrm{tr}\mathbb{D}_W(\mathbf{x}))\cdot\frac{\boldsymbol{\theta}^t\mathbb{D}_W(\mathbf{x})\boldsymbol{\theta}}{(\mathrm{tr}\mathbb{D}_W(\mathbf{x}))^2} + (\mathrm{tr}\mathbb{D}_W(\mathbf{x}))^{-1}\cdot\nabla_{\mathbf{x}}\left(\sum_{k,l=1}^{n} d_w^{kl}(\mathbf{x})\theta^k\theta^l\right)\\
&= \frac{-1}{\mathrm{tr}\mathbb{D}_W(\mathbf{x})}\left[\begin{pmatrix}\partial_{x_1}(\mathrm{tr}\mathbb{D}_W(\mathbf{x}))\\ \vdots\\ \partial_{x_n}(\mathrm{tr}\mathbb{D}_W(\mathbf{x}))\end{pmatrix}\frac{\boldsymbol{\theta}^t\mathbb{D}_W(\mathbf{x})\boldsymbol{\theta}}{\mathrm{tr}\mathbb{D}_W(\mathbf{x})} - \begin{pmatrix}\sum_{k,l=1}^{n}\partial_{x_1}d_w^{kl}(\mathbf{x})\theta^k\theta^l\\ \vdots\\ \sum_{k,l=1}^{n}\partial_{x_n}d_w^{kl}(\mathbf{x})\theta^k\theta^l\end{pmatrix}\right].
\end{aligned}$$

[2] the larger the value of κ, the higher the concentration of distribution around the mean direction.

So this is a vector $\gamma(\mathbf{x}) = (\gamma_1(\mathbf{x}), \dots, \gamma_n(\mathbf{x}))^t$ with

$$\gamma_i(\mathbf{x}) = \frac{-1}{(\mathrm{tr}\mathbb{D}_W(\mathbf{x}))^2}\partial_{x_i}(\mathrm{tr}\mathbb{D}_W(\mathbf{x}))\,\boldsymbol{\theta}^t\mathbb{D}_W(\mathbf{x})\boldsymbol{\theta} + \frac{1}{\mathrm{tr}\mathbb{D}_W(\mathbf{x})}\sum_{k,l=1}^{n}\partial_{x_i}d_w^{kl}(\mathbf{x})\theta^k\theta^l.$$

From this observe that

$$\int_V \boldsymbol{\theta}\boldsymbol{\theta}^t \nabla\left(\frac{1}{\mathrm{tr}\mathbb{D}_W(\mathbf{x})}\boldsymbol{\theta}^t\mathbb{D}_W(\mathbf{x})\boldsymbol{\theta}\right)d\boldsymbol{\theta}$$

is a vector $\alpha(\mathbf{x}) = \big(\alpha_1(\mathbf{x}), \dots, \alpha_n(\mathbf{x})\big)^t$ with components

$$\begin{aligned}
\alpha_c(\mathbf{x}) &= \int_V \sum_{d=1}^{n}\theta^c\theta^d\left(\frac{-1}{(\mathrm{tr}\mathbb{D}_W(\mathbf{x}))^2}\partial_{x_d}\big(\mathrm{tr}\mathbb{D}_W(\mathbf{x})\big)\sum_{a,b=1}^{n}\theta^a\theta^b d_w^{ab}(\mathbf{x})\right.\\
&\quad\left.+\frac{1}{\mathrm{tr}\mathbb{D}_W(\mathbf{x})}\sum_{a,b=1}^{n}\partial_{x_d}d_w^{ab}(\mathbf{x})\theta^a\theta^b\right)d\theta\\
&= -\frac{1}{(\mathrm{tr}\mathbb{D}_W(\mathbf{x}))^2}\left(\sum_{d,a,b=1}^{n}\partial_{x_d}\big(\mathrm{tr}\mathbb{D}_W(\mathbf{x})\big)d_w^{ab}(\mathbf{x})\int_V\theta^c\theta^d\theta^a\theta^b d\theta\right)\\
&\quad+\frac{1}{\mathrm{tr}\mathbb{D}_W(\mathbf{x})}\left(\sum_{d,a,b=1}^{n}\partial_{x_d}d_w^{ab}(\mathbf{x})\int_V\theta^c\theta^d\theta^a\theta^b d\theta\right)\\
&:= \alpha_c^1(\mathbf{x}) + \alpha_c^2(\mathbf{x}).
\end{aligned}$$

Now we evaluate the two terms above. For this recall (Hillen 2005) that

$$\int_V \theta^c\theta^d\theta^a\theta^b d\theta = \frac{\omega_n}{n(n+2)}\big(\delta^{cd}\delta^{ab} + \delta^{ca}\delta^{db} + \delta^{cb}\delta^{da}\big),$$

hence

$$\begin{aligned}
\alpha_c^1(\mathbf{x}) &= -\frac{1}{(\mathrm{tr}\mathbb{D}_W(\mathbf{x}))^2}\frac{\omega_n}{n(n+2)}\\
&\quad\left(\sum_{d,a,b=1}^{n}\partial_{x_d}\big(\mathrm{tr}\mathbb{D}_W(\mathbf{x})\big)d_w^{ab}(\mathbf{x})\big(\delta^{cd}\delta^{ab}+\delta^{ca}\delta^{db}+\delta^{cb}\delta^{da}\big)\right)\\
&= -\frac{1}{(\mathrm{tr}\mathbb{D}_W(\mathbf{x}))^2}\frac{\omega_n}{n(n+2)}\left(\sum_{d,a,b=1}^{n}\partial_{x_d}\big(\mathrm{tr}\mathbb{D}_W(\mathbf{x})\big)d_w^{ab}(\mathbf{x})\delta^{cd}\delta^{ab}\right.\\
&\quad\left.+\sum_{d,a,b=1}^{n}\partial_{x_d}\big(\mathrm{tr}\mathbb{D}_W(\mathbf{x})\big)d_w^{ab}(\mathbf{x})\delta^{ca}\delta^{db}+\sum_{d,a,b=1}^{n}\partial_{x_d}\big(\mathrm{tr}\mathbb{D}_W(\mathbf{x})\big)d_w^{ab}(\mathbf{x})\delta^{cb}\delta^{da}\right)
\end{aligned}$$

$$= -\frac{1}{(\mathrm{tr}\mathbb{D}_W(\mathbf{x}))^2}\frac{\omega_n}{n(n+2)}\Bigg(\sum_{d=1}^{n}\partial_{x_d}\big(\mathrm{tr}\mathbb{D}_W(\mathbf{x})\big)\delta^{cd}\mathrm{tr}\mathbb{D}_W(\mathbf{x}) + \sum_{d=1}^{n}\partial_{x_d}\big(\mathrm{tr}\mathbb{D}_W(\mathbf{x})\big)d_w^{cd}(\mathbf{x}) + \sum_{d=1}^{n}\partial_{x_d}\big(\mathrm{tr}\mathbb{D}_W(\mathbf{x})\big)d_w^{dc}(\mathbf{x})\Bigg).$$

Hence, we obtain for the vector $\alpha^1(\mathbf{x})$:

$$-\frac{1}{(\mathrm{tr}\mathbb{D}_W(\mathbf{x}))^2}\frac{\omega_n}{n(n+2)}\Bigg(\mathrm{tr}\mathbb{D}_W(\mathbf{x})\mathbb{I}_n + 2\mathbb{D}_W(\mathbf{x})\Bigg)\cdot\nabla\mathrm{tr}\mathbb{D}_{\mathbf{W}}(\mathbf{x}).$$

Analogously, we obtain for $\alpha_c^2(\mathbf{x})$:

$$\begin{aligned}\alpha_c^2(\mathbf{x}) &= \frac{1}{\mathrm{tr}\mathbb{D}_W(\mathbf{x})}\frac{\omega_n}{n(n+2)}\Bigg(\sum_{d,a,b=1}^{n}\partial_{x_d}d_w^{ab}(\mathbf{x})\big(\delta^{cd}\delta^{ab}+\delta^{ca}\delta^{db}+\delta^{cb}\delta^{da}\big)\Bigg)\\ &= \frac{1}{\mathrm{tr}\mathbb{D}_W(\mathbf{x})}\frac{\omega_n}{n(n+2)}\Bigg(\sum_{d,a,b=1}^{n}\partial_{x_d}d_w^{ab}(\mathbf{x})\delta^{cd}\delta^{ab} + \sum_{d,a,b=1}^{n}\partial_{x_d}d_w^{ab}(\mathbf{x})\delta^{ca}\delta^{db} + \sum_{d,a,b=1}^{n}\partial_{x_d}d_w^{ab}(\mathbf{x})\delta^{cb}\delta^{da}\Bigg)\\ &= \frac{1}{\mathrm{tr}\mathbb{D}_W(\mathbf{x})}\frac{\omega_n}{n(n+2)}\Bigg(\sum_{a=1}^{n}\partial_{x_c}d_w^{aa}(\mathbf{x}) + \sum_{d=1}^{n}\partial_{x_d}d_w^{cd}(\mathbf{x}) + \sum_{d=1}^{n}\partial_{x_d}d_w^{dc}(\mathbf{x})\Bigg),\end{aligned}$$

and this means

$$\alpha^2(\mathbf{x}) = \frac{1}{\mathrm{tr}\mathbb{D}_W(\mathbf{x})}\frac{\omega_n}{n(n+2)}\Bigg(\nabla\mathrm{tr}\mathbb{D}_W(\mathbf{x}) + 2\nabla\cdot\mathbb{D}_W(\mathbf{x})\Bigg).$$

Altogether, this yields

$$\begin{aligned}\mathbf{u}(\mathbf{x}) &= \frac{s^2}{\lambda_0(n+2)}\Bigg[-\frac{1}{(\mathrm{tr}\mathbb{D}_W(\mathbf{x}))^2}\Bigg(\mathrm{tr}\mathbb{D}_W(\mathbf{x})\mathbb{I}_n + 2\mathbb{D}_W(\mathbf{x})\Bigg)\cdot\nabla\mathrm{tr}\mathbb{D}_{\mathbf{W}}(\mathbf{x})\\ &\quad + \frac{1}{\mathrm{tr}\mathbb{D}_W(\mathbf{x})}\Bigg(\nabla\mathrm{tr}\mathbb{D}_W(\mathbf{x}) + 2\nabla\cdot\mathbb{D}_W(\mathbf{x})\Bigg)\Bigg] \qquad (25)\\ &= \frac{2s^2}{\lambda_0(n+2)}\Bigg(\frac{\nabla\cdot\mathbb{D}_W(\mathbf{x})}{\mathrm{tr}\mathbb{D}_W(\mathbf{x})} - \frac{\mathbb{D}_W(\mathbf{x})\cdot\nabla\mathrm{tr}\mathbb{D}_{\mathbf{W}}(\mathbf{x})}{(\mathrm{tr}\mathbb{D}_W(\mathbf{x}))^{\mathbf{2}}}\Bigg). \qquad (26)\end{aligned}$$

2.5 Complete macroscopic model

We summarize our model to bring it into a more compact form. We derived the evolution equation

$$\partial_t M_0 - \nabla \cdot (\mathbb{D}_T(\mathbf{x})\nabla M_0) + \nabla \cdot ([g(A(\mathbf{x}))\mathbb{D}_T(\mathbf{x})\nabla A(\mathbf{x}) - \mathbf{u}(\mathbf{x})]\, M_0) = 0 \quad (27)$$

for the macroscopic quantity $M_0(t, \mathbf{x})$ where $g(A(\mathbf{x}))$ is as in (8). We employed

$$q(\mathbf{x}, \boldsymbol{\theta}) = \frac{n}{|\mathbb{S}^{n-1}|\mathrm{tr}\mathbb{D}_W(\mathbf{x})}\boldsymbol{\theta}^t \mathbb{D}_W(\mathbf{x})\boldsymbol{\theta}$$

to derive explicit terms for the coefficients $\mathbb{D}_T(\mathbf{x})$ and $\mathbf{u}(\mathbf{x})$ which led to

$$\mathbb{D}_T(\mathbf{x}) = \frac{s^2}{\lambda_0(n+2)}\left(\mathbb{I}_n + 2\frac{\mathbb{D}_W(\mathbf{x})}{\mathrm{tr}\mathbb{D}_W(\mathbf{x})}\right), \quad (28)$$

and

$$\mathbf{u}(\mathbf{x}) = \frac{2s^2}{\lambda_0(n+2)}\left(\frac{\nabla \cdot \mathbb{D}_W(\mathbf{x})}{\mathrm{tr}\mathbb{D}_W(\mathbf{x})} - \frac{\mathbb{D}_W(\mathbf{x}) \cdot \nabla \mathrm{tr}\mathbb{D}_\mathbf{W}(\mathbf{x})}{(\mathrm{tr}\mathbb{D}_W(\mathbf{x}))^\mathbf{2}}\right), \quad (29)$$

where the values of the water diffusion tensor $\mathbb{D}_W(\mathbf{x})$ are known from DTI measurements. We want to simulate this equation numerically in the next section and for reasons of clarity and comprehensibility rewrite it in the form

$$\partial_t M_0 - \nabla \cdot (\mathbb{D}_T(\mathbf{x})\nabla M_0) - \nabla \cdot (\mathbf{v}(\mathbf{x})\, M_0) = 0, \quad (30)$$

with $\mathbf{v}(\mathbf{x}) := \mathbf{u}(\mathbf{x}) - g(A(\mathbf{x}))\mathbb{D}_T(\mathbf{x})\nabla A(\mathbf{x})$.

3 Numerical simulations

We present 2D simulations of the resulting macroscopic advection-diffusion equation (30). The tumor diffusion tensor and the tumor drift velocity are precalculated in the MATLAB[3] numerics software. The simulations of the macroscopic evolution equation are implemented using the DUNE framework (Bastian et al. 2008).

The macroscopic quantities $\mathbb{D}_T(\mathbf{x})$ and $\mathbf{v}(\mathbf{x})$ are spatially dependent, and we expect regions in space where the system is diffusion dominated and regions where it is drift dominated. This can be expressed by the spatially dependent Péclet number $\mathrm{Pe} = \frac{\|\mathbf{v}(\mathbf{x})L\|}{\|\mathbb{D}_T(\mathbf{x})\|}$, where the norm in the numerator is the L^2 norm, while we take in the denominator the Frobenius norm of $\mathbb{D}_T$. L is a macroscopic characteristic length scale (2 mm, in our present setting and simulations). For $\mathrm{Pe} \ll 1$ we have a diffusion dominated case, and classical methods for parabolic equations will apply, while for $\mathrm{Pe} \gg 1$ the equation is drift dominated, and hyperbolic numerical methods need to

[3] MATLAB Release 2012b, The MathWorks, Inc., Natick, Massachusetts, United States.

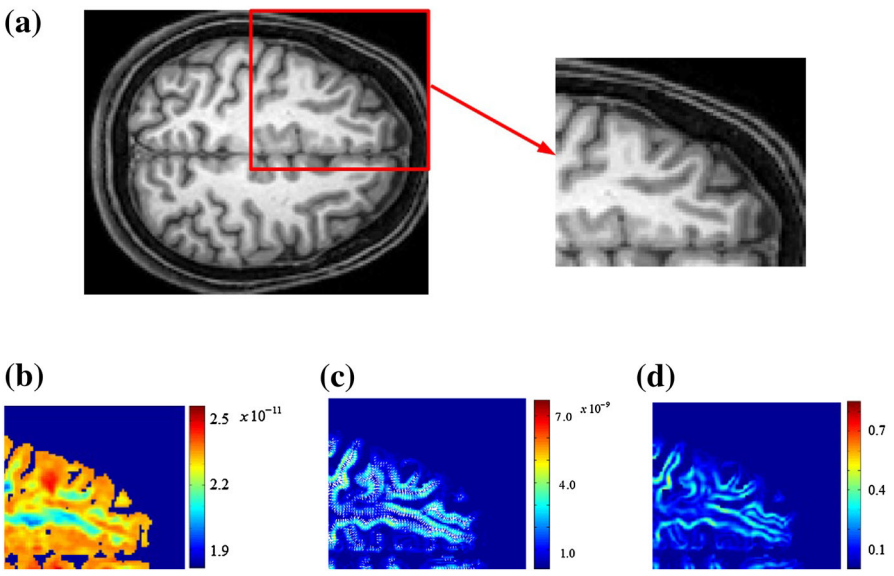

Fig. 4 Visualization of the local invasive behaviour. **a** For the visualization we focus on the selected right upper part of the brain slice. **b** Local Frobenius norm of the tumor diffusion tensor. **c** Quiver plot of the drift term resulting from internal dynamics. White matter regions with a high anisotropy lead to higher velocities. **d** Local Péclet number Pe, indicates where the migration is dominated by diffusion and where by advection Vizualization of the local invasive behavior

be used. Note that the equation is still parabolic, but the numerical method should be chosen based on its characteristics scales. In Fig. 4b we illustrate the behavior of the Frobenius norm of $\mathbb{D}_T(\mathbf{x})$. That of the Péclet number is shown in Fig. 4d. We clearly observe a large Péclet number along the white matter tracks.

The numerical scheme needs to be able to handle degenerated anisotropic parabolic equations and full tensors. Furthermore it should be locally mass conservative. For these reasons we decided to employ a first order discontinuous Galerkin (dG) scheme in space and an implicit Euler scheme in time. This method is overall first order accurate.

3.1 Discretization

For the simulation we use a structured mesh $\mathcal{M}(\Omega) = \{E_i\}$, which is a subset of the voxel mesh of the DTI data. Since our mesh is Cartesian with mesh-width h, the sets E_i are simply the grid cells that belong to the brain tissue. We define the skeleton of $\mathcal{M}$ as the boundary between those grid cells, $\Gamma = \left\{\gamma_{e,f} = \partial E_e \cap \partial E_f \;\middle|\; E_e, E_f \in \mathcal{M},\ E_e \neq E_f, \text{ and } |\gamma_{e,f}| > 0\right\}$.

We first discuss the spatial discretization. We use a symmetric interior penalty discontinuous Galerkin method (SIPG) (Wheeler 1978) as implemented in DUNE (Bastian et al. 2008). We denote with V_h the discontinuous Galerkin Ansatz-space, which is in our case the space of piecewise bilinear polynomials

$$V_h = \left\{ v_h \in L^2(\Omega) \,:\, v_h|_E \in Q_1(E), E \in \mathcal{M}(\Omega) \right\},$$

where $Q_1(E)$ denotes the set of bi-linear functions on E. We test the above equation (30) with these ansatz functions, use a weak formulation, and express coupling conditions along the skeleton through jumps $[\![\cdot]\!]$ and averages $\{ \cdot \}$ in a similar notation as introduced by Arnold et al. (2002). We use weighted averages, as proposed in Ern et al. (2009). Omitting the computational details, which can be found for example in Arnold et al. (2002), the resulting semi-discrete problem reads: Find $M_{0h}(t) \in V_h$ such that

$$\partial_t M_{0h}(t) + a_h\big(M_{0h}(t), v_h\big) + J_h\big(M_{0h}(t), v_h\big) = 0 \qquad \forall v_h \in V_h, \tag{31}$$

with the bilinear form a_h and a penalty term J_h given by

$$\begin{aligned} a_h\big(M_{0h}(t), v_h\big) = &\int_\Omega \mathbb{D}_T \nabla M_{0h}(t) \cdot \nabla v_h \, dx - \int_\Gamma [\![M_{0h}(t)]\!] \cdot \{ \mathbb{D}_T \nabla v_h \} \\ &+ [\![v_h]\!] \cdot \{ \mathbb{D}_T \nabla M_{0h}(t) \} \, ds - \int_\Omega \mathbf{v} \, M_{0h}(t) \, \nabla v_h \, dx \\ &+ \int_\Gamma [\![v_h]\!] \cdot \mathbf{v} \, M_{0h}^{\uparrow}(t) ds. \end{aligned} \tag{32}$$

and

$$J_h\big(M_{0h}(t), v_h\big) = \eta h^{-1} \int_\Gamma [\![M_{0h}]\!] [\![v_h]\!] \, ds \,, \tag{33}$$

where $\eta > 0$ denotes the penalty factor. For a good choice of η we refer to (Ern et al. 2009).

Note that we require the normal velocity to be continuous, i.e. $\mathbf{v}|_{\partial E_n} \mathbf{n}_n = -\mathbf{v}|_{\partial E_m} \mathbf{n}_m$, where $\mathbf{n}_n$ denotes the outer normal vector of grid cell E_n. To ensure this, we use a Raviart-Thomas RT0 approximation of the velocity field. On an internal edge with two adjacent cells E_n and E_m we define $[\![x]\!] = x|_{\partial E_n} \mathbf{n}_n + x|_{\partial E_m} \mathbf{n}_m$ and $\{ x \} = \omega_n x|_{\partial E_n} + \omega_m x|_{\partial E_m}$, with weights ω_n, ω_m and the unit outer normal vectors $\mathbf{n}_n, \mathbf{n}_m$. To be robust with respect to heterogeneous diffusion coefficients, we use the weights $\omega_n = \frac{\mathbf{n}_n^t \mathbb{D}_{Tn} \mathbf{n}_n}{\mathbf{n}_n^t (\mathbb{D}_{Tn} + \mathbb{D}_{Tm}) \mathbf{n}_n}$ and $\omega_m = \frac{\mathbf{n}_m^t \mathbb{D}_{Tm} \mathbf{n}_m}{\mathbf{n}_m^t (\mathbb{D}_{Tn} + \mathbb{D}_{Tm}) \mathbf{n}_m}$ respectively, where $\mathbb{D}_{Tn}$ denotes the tumour diffusion tensor computed in E_n. Note that due to $\mathbf{n}_n = -\mathbf{n}_m$ the relation $\omega_n + \omega_m = 1$ holds.

The advective term is stabilized using an upwind formulation, with the upwind reconstruction $M_{0h}^{\uparrow}$ of the cell density.

For the time discretization of M_{0h} we used an implicit Euler scheme and time steps τ such that we fulfill a CFL (Courant-Friedrichs-Lewy) condition of 1.

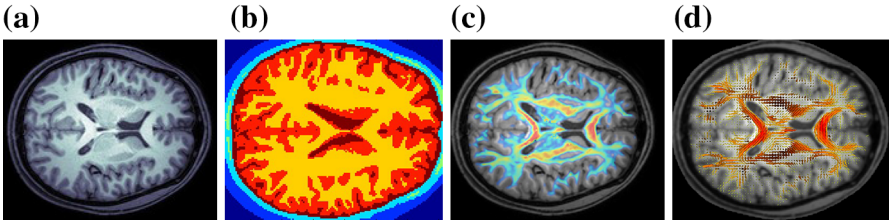

Fig. 5 Scanned and processed MRI brain data of a healty young male subject. **a** T1 weighted picture of a brain slice. **b** Segmentation of the brain slice. **c** Overlay of fractional anisotropy and T1 picture. **d** Visualization of the main direction of diffusion by a vector pointing in the direction of the tensor's leading eigenvalue

Table 1 Choice of parameters which cannot be obtained from MRI data

Parameter	Value	Source
R_0	10^5	Belkin et al. (2005)
s	$10^{-6}\,\mathrm{m\,s^{-1}}$	Sidani et al. (2007)
λ_0	$0.1\,\mathrm{s^{-1}}$	Sidani et al. (2007)
λ_1	$0.01\,\mathrm{s^{-1}}$	Estimated
k^+	$0.1\,\mathrm{s^{-1}}$	Estimated
k^-	$0.1\,\mathrm{s^{-1}}$	Lauffenburger and Lindermann (1993)

3.2 Extraction of the model parameters

The parameters used in the simulations are collected in the following table.[4]

The parameters for $\mathbb{D}_T$ and $\mathbf{v}$, as well as the computational domain Ω are obtained from 3D MRI data. MRI measurements yield a T1 image and DTI data (see Fig. 5) on a domain $\hat{\Omega}$, including the whole skull and brain. The T1 image (Fig. 5a) shows regions of gray and white matter and image segmentation yields the actual computational domain Ω as the union of these tissues, depicted in yellow and light red color (Fig. 5b).

The coefficients of $\mathbb{D}_T$ and $\mathbf{v}$ are reconstructed from 3D DTI data using finite-difference approximations of the derivatives. These quantities were then projected onto the 2D simulation slice. It is assumed that the volume fraction A of ECM is high where the tissue is strongly aligned and thus we observe a high anisotropy in $\mathbb{D}_W(\mathbf{x})$. For this reason we use the *fractional anisotropy* index (introduced in Sect. 1.2) as a measure for A. Figure 5c shows the fractional anisotropy index for the water diffusion tensor and 5d visualizes the largest eigenvector, i.e., the main direction.

Gradients of $\mathbb{D}_W(\mathbf{x})$ and A are computed on a staggered grid and the resulting velocity field is projected onto an RT0 approximation on the original voxel grid.

[4] We assumed that attachment and detachment of receptors to tissue components take place with similar rates. However, variations in the choice of the binding rate k^+ (we tried with up to 50 %) do not seem to influence the dynamics in a notable way. The choice of λ_1 is rather imprecise, as there are no data or references available for this parameter. We took it to be rather small, in order to endorse the positivity of the turning rate and not to exaggerate the influence of the microscale dynamics. Larger values of λ_1 would mean higher advection, hence a more pronounced anisotropic behavior.

The choice for the parameters s, R_0, $\lambda_0\,\lambda_1$, k^+ and k^- can be found in Table 1, where we also cited some biological relevant sources for the parameter choice, or marked where we estimated the values. Note that a specific choice of s results only in time scaling of the simulation. We tested variations of these parameters by $\pm 50\,\%$ and we found very similar simulation behavior. The spread pattern might develop slower or faster, but the overall spread patterns are very similar to each other.

3.3 Simulation results

In the following we compare simulations done with and without the supplementary advection term involving $g(A(\mathbf{x}))\mathbb{D}_T(\mathbf{x})\nabla A(\mathbf{x})$ and which is due to our accounting for subcellular dynamics.

Figure 6 illustrates the numerical simulation of the evolution equation for cancer cells without the mentioned advective term. The effect of anisotropic diffusion shows as expected a dependence on direction. We started our simulations with a binary distribution; a small initial tumor is located in the left hemisphere of the brain.

Figure 7 shows the evolution of the tumor cell density with prevalent advective effects originating from the subcellular dynamics and considering a turning rate depending on these dynamics. The results differ significantly from diffusion dominated spread and the underlying tissue structure is visible. We will return to this point later in Sect. 4.

We also compared in Fig. 8 the simulation results for the two suggested choices (22) and (23) for the fibre distribution function q. The tumor evolution at the endstep $t = 200 \times 10^6$ s is shown for the peanut distribution function (first column in Fig. 8) and for the von Mises-Fisher distribution (last two columns in the figure) for the values $\kappa = 10$ and $\kappa = 20$, both for the diffusion dominated case (upper row) and for the full system with advective terms involving subcellular dynamics (lower row). As expected, an increased κ leads to a higher degree of anisotropy in the spread.

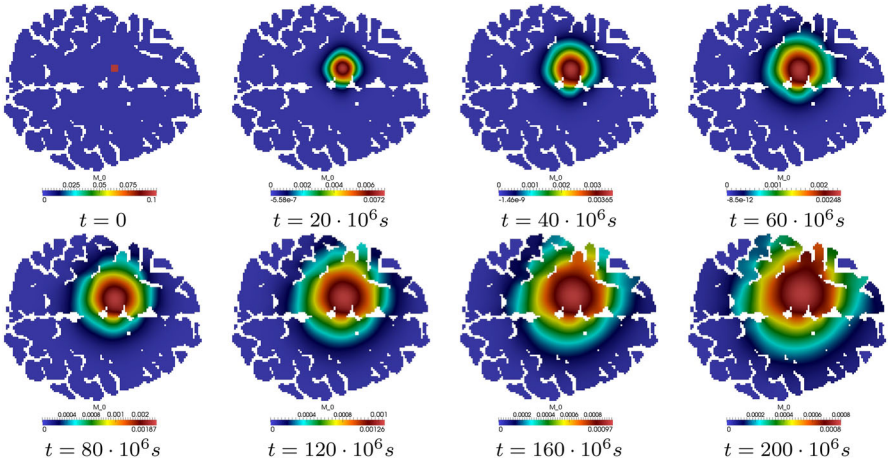

Fig. 6 Spread of cancer cells in the brain: case not involving subcellular dynamics

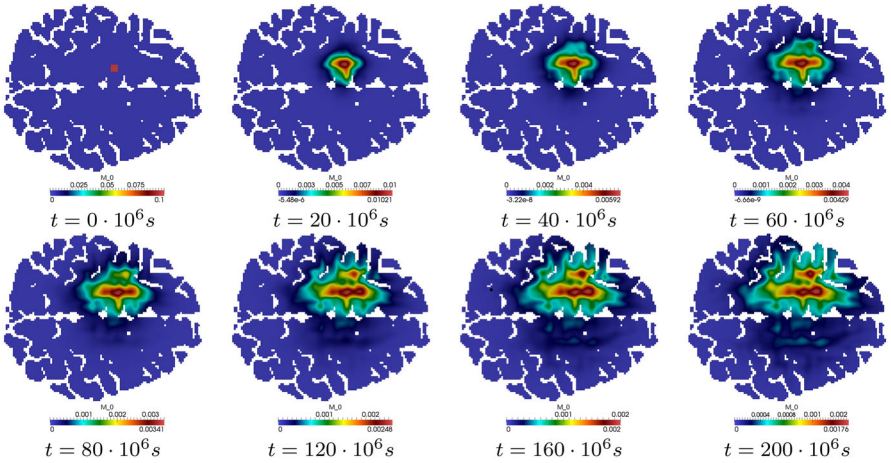

Fig. 7 Spread of cancer cells in the brain: advection dominated case (subcellular dynamics involved). For the parameters see Table 1

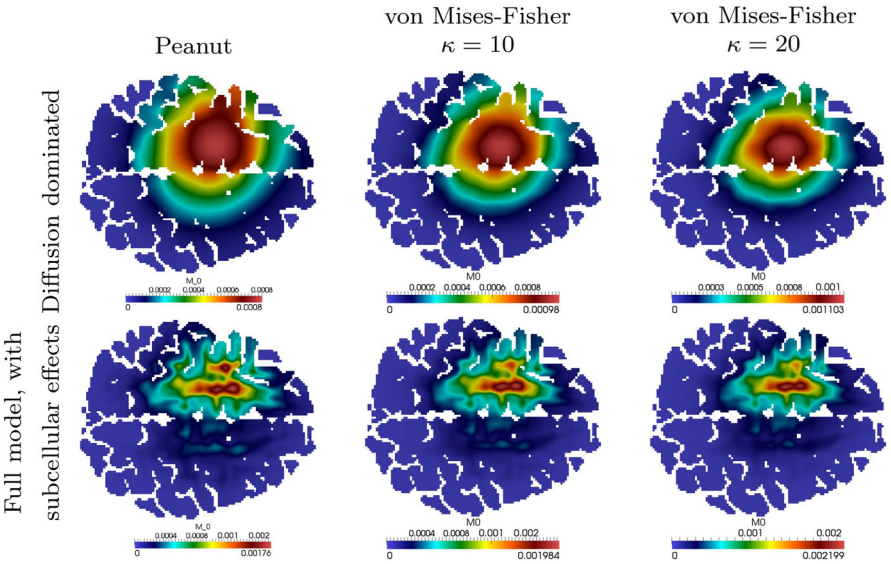

Fig. 8 Comparison of the spread of cancer cells in the brain for the distribution (22) and the bimodal von Mises-Fisher distribution (23) at the endstep $t = 200 \times 10^6$ s. For the parameters see Table 1

Nevertheless, the results for the tumor evolution look quite similar when compared to each other. This suggests that the additional drift term resulting from the integrin dynamics has the predominant effect, and the particular type of diffusion plays a minor role in generating anisotropic growth patterns.

4 Discussion

Multiscale models make it possible to understand cancer cell migration in greater detail. Thereby, micro- and mesoscopic aspects like subcellular dynamics and individual interactions of cells with the surrounding tissue network can be used to render modeling more precise than descriptions made directly on the macroscopic scale. Our model on the microscale is a differential equation for the cell surface receptors binding to the tissue. Including this subcellular dynamics led to an additional convection term in the transport equation on the macroscale. The latter was deduced by a parabolic scaling performed on the originary kinetic transport model. The resulting equation (21) for the macroscopic tumor cell density M_0 is of advection-diffusion type. Thereby, the tumor diffusion tensor $\mathbb{D}_T(\mathbf{x})$ contains information about the local tissue structure, as it depends on the fibre distribution function q. The dynamics on the microscale are then involved in a haptotactic drift term, corresponding to a directed movement of cancer cells along the gradient of ECM density.

With a special choice for the form of the fibre distribution allowing to take also DTI data into account we were able to determine the specific structure of the diffusion tensor and drift velocity explicitly. Since both only depend on the values of the water diffusion tensor $\mathbb{D}_W(\mathbf{x})$ for each voxel, they can be easily evaluated.

Numerical simulations for the equation obtained in Subsect. 2.5 have been performed within a domain representing a single slice of a human brain and showed that our model predicts a highly anisotropic spread of the tumor in the surrounding tissue. A comparison of simulations with and without drift indicated that the influence of the haptotactic drift term (essentially involving the receptor dynamics on the cell surface) is striking. It can be seen that within tissue areas with a lot of aligned fibre bundles the tumor spreads along these structures. This observation supports the conjecture that directed cellular movement plays a crucial role in cancer invasion processes, while diffusion is seen as a driving factor of the cell dispersal. This makes sense from the biological point of view, since haptotactic and chemotactic movements of cells are assumed to be the major transport mechanisms on the cellular scale. Our model bridges the scales from the subcellular level of receptor binding (which can be seen as the onset of all subsequent processes related to cell motility, see e.g., Hood and Cheresh 2002) over the mesoscale of individual cell behavior in interaction with the tissue and up to the macroscale of the tumor population. Thus, the latter is directly connected to the dynamics on the subcellular scale, which are actually driving the motility and proliferation of cells and hence the growth and spread of the cancer (Hanahan and Weinberg 2011). As mentioned, the equation for the macroscopic cell density involves in its coefficients the tumor diffusion tensor and the drift velocity, both explicitly computed from DTI data, the cell speeds, and the cell turning rates. Moreover, it carries—again in an explicit way—the subcellular information about receptor binding dynamics. The resulting additional advective-type term endorses in the simulations the well known fact that glioma follow white matter tracts (D'Abaco and Kaye 2007; Claes et al. 2007; Giese and Kluwe 1996; Giese and Westphal 1996) and is, moreover, able to

describe[5] the finger-like and sometimes fibrillary invasion patterns for glioma, as observed in clinical practice, see e.g., Coons (1999); Daumas-Duport et al. (1997); Gerstner et al. (2010); Matsukado et al. (1961). The latter could not be obtained so far with the more common (reaction-)diffusion based models, see e.g., Jbabdi et al. (2005); Cobzas et al. (2009); Konukoglu et al. (2010) set directly on the macroscopic scale. While diffusion is driving the cells spread, it is the drift term in Eq. (21) (and its effect is decisively enhanced by the term involving $g(A(\mathbf{x}))$, hence the microlevel dynamics) who is directing their motion according to the local tissue anisotropy.

Painter and Hillen (2013) questioned the choice (22) for the fibre distribution and proposed instead the von Mises-Fisher distribution (23). Thus we carried out a numerical comparison between the two choices both with and without subcellular dynamics. We found that the simulations without subcellular dynamics are diffusion dominated for both choices (22) and (23), whereas involving integrin binding and the corresponding turning rate led to pronounced advection and strongly anisotropic distribution of tumor cells.

As shown in Sect. 3, the dominating process (advection or diffusion) differs locally, thus it is important to use numerical schemes, which can handle degenerated parabolic equations. Methods like discontinuous Galerkin and finite volume schemes are particularly attractive, as they fulfil this requirement and are locally mass conservative. In order to efficiently handle 3D simulations and sharp fronts, higher order methods with flux limiters should be considered.

Several open problems and questions remain, rendering future work necessary. In our model many biological relevant processes are still missing or are highly simplified. For instance, we neglected the influence of chemotactic movement of the cells due to their response to matrix degrading enzymes and we did not take proliferation into account. While chemotaxis can be integrated as in the works of Kelkel and Surulescu (2011) and Kelkel and Surulescu (2012), it is still unclear how to introduce proliferation on the level of mesoscopic dynamics in an appropriate way also allowing for reliable numerical simulations. Some suggestions have been made by Bellomo et al. (2010) in the KTAP framework, however, they rely on cell–cell interaction as a necessary condition for proliferation and it is still not clear how to deduce the macroscopic limit in that context. When modeling directly on the macroscopic level, this is a less challenging issue, as one can simply add a source term (e.g., logistic growth with or without crowding) in the right hand side of the equation in Subsect. 2.5. This approach is, however, rather artificial, as the form of the source term is directly imposed by some 'guess' and not mathematically deduced from considerations involving relevant processes on the lower scales. This and further issues are addressed in a forthcoming paper.

For the sake of simplicity, we did not consider manipulative interactions of the cells with the underlying tissue network, although there are several important aspects. While moving, cells use proteolytic enzymes to degrade bundles of collagen fibres detainig their movement. This effect has already been taken into account (Hillen 2006; Kelkel and Surulescu 2011, 2012) and calls for an additional evolution equation for the fibre

[5] at least qualitatively, till data become available for an adequate validation.

density which has been assumed to be constant in time in our model. Additionally, there is a displacement of healthy tissue due to the growing volume of the tumor. This effect has also been neglected, but could also be embedded in our model, e.g., by the already mentioned equation for tissue fibre density or by a supplementary evolution equation for healthy cells.

We also mentioned that the tensor model encompasses some significant shortcomings. One of its main underlying assumptions is that diffusion is Gaussian and it has six degrees of freedom. Hence, the tensor model is unable to resolve crossing fibre bundles within a voxel. For many applications new imaging techniques with higher angular resolution (e.g., HARDI) techniques are needed. Modern HARDI techniques as Q-ball imaging make it possible to resolve the neural fibre structure in much more detail. It seems to be promising to use these methods in the numerical simulations instead of the tensor data.

Furthermore, the question of how to relate DTI data to neural fibre structure is a nontrivial one, and obviously this relationship cannot be represented by a simple mathematical expression of the form (22) or (23). Hence, it is necessary to find an approximation which is mathematically simple, yet contains enough information. An option would be to use methods from the field of tractography, which is concerned with identifying neural tracts by using DTI data (Descoteaux 2008; Descoteaux et al. 2009).

Besides these modeling issues there are some interesting problems also w.r.t. mathematical analysis: the deduction of the macroscopic limit would need a rigorous proof, which is a nontrivial issue. The existence and uniqueness of a positive solution to the kinetic transport equation coupled with the subcellular dynamics can be done by relying on the result by Kelkel and Surulescu (2012), where an even more complex multiscale model for tumor cell migration has been proposed and analyzed. Thereby, the existence proof needed the regularity assumption L^∞ on the entire, particularly unbounded space of positions, velocities and internal states and to our knowledge this assumption is needed also for the other existing results concerning multiscale models of this type. Recently, see Lorenz and Surulescu (2014), this condition has been weakened and a global existence and uniqueness result in L^2 spaces has been obtained in a much more general context, in which the model presented here and the one in Ref. (Kelkel and Surulescu 2012) are just particular cases.

Eventually, we stress out that taking subcellular processes into account leads to an additional advective term on the macroscale, which has non negligible influence on the spatial distribution of the tumor cells. In order to precisely assess the relevance of this term in comparison to recent standard models, suitable experimental data would be necessary for a validation.

Acknowledgments We thank Carsten Wolters and Felix Lucka (Institute of Biomagnetism and Biosignalanalysis, University of Münster) for a lot of preprocessed DTI data and much advice with the visualization software SciRun. We are grateful for supportive and challenging remarks by Andreas Deutsch (TU Dresden) and for enlightening discussions with Katarina Wolf (Radboud University Nijmegen) concerning the biology of glioma invasion.

References

Alt W (1980) Biased random walk models for chemotaxis and related diffusion approximations. J Math Biol 9:147–177

Anderson A, Chaplain M, Newman E, Steele R, Thompson A (2000) Mathematical modeling of tumor invasion and metastasis. J Theor Med 2:129–154

Arnold DN, Brezzi F, Cockburn B, Marini LD (2002) Unified analysis of discontinuous galerkin methods for elliptic problems. SIAM J Numer Anal 39(5):1749–1779

Barocas V, Tranquillo R (1997) An anisotropic biphasic theory of tissue-equivalent mechanics: the interplay among cell traction, fibrillar network deformation, firbil alignment and cell contact guidance. ASME J Biomech Eng 119:137–145

Basser P, Matiello J, LeBihan D (1992) Diagonal and off-diagonal components of the self-diffusion tensor: their relation to and estimation from the NMR spin-echo signal, 11th Society of Magnetic Resonance in Medicine Meeting 1222

Basser P, Matiello J, Turner R, LeBihan D (1993) Diffusion tensor echo-planar imaging of human brain. In: Proceedings of the SMRM 584

Bastian P, Blatt M, Dedner A, Engwer C, Klöfkorn R, Kornhuber R, Ohlberger M, Sander O (2008) A generic grid interface for parallel and adaptive scientific computing. Part II: implementation and tests in DUNE. Computing 82(2–3):121–138

Belkin A, Tsurupa G, Zemskov E, Veklich Y, Weisel J, Medved L (2005) Transglutaminase-mediated oligomerization of the fibrin(ogen) αC domains promotes integrin-dependent cell adhesion and signaling. Blood 105(9):3561–3568

Bellomo N, Bellouquid A, Nieto J, Soler J (2010) Complexity and mathematical tools toward the modeling of multicellular growing systems. Math Comput Model 51:441–451

Beppu T, Inoue T, Shibata Y, Kurose A, Arai H, Ogasawara K, Ogawa A, Nakamura S, Kabasawa H (2003) Measurement of fractional anisotropy using diffuson tensor MRI in supratentorial astrocytic tumors. J Neuro Oncol 63:109–116

Bondiau P, Clatz O, Sermesant M, Marcy P, Delingette H, Frenay M, Ayache N (2008) Biocomputing: numerical simulation of glioblastoma growth using diffusion tensor imaging. Phys Med Biol 53:879–893

Bournaveas N, Calvez V (2008) Global existence for the kinetic chemotaxis model without pointwise memory effects, and including internal variables. Kinetic Related Models 1:29–48

Chalub F, Markovich P, Perthame B, Schmeiser C (2004) Kinetic models for chemotaxis and their drift-diffusion limits. Monatshefte für Mathematik 142(1–2):123–141

Chaplain M, Lolas G (2006) Mathematical modelling of cancer invasion of tissue: dynamic heterogeneity. Netw Heterog Media 1:399–439

Chauviere A, Preziosi L (2010) Mathematical framework to model migration of cell population in extracellular matrix, Chapter. In: Chauviere A, Preziosi L, Verdier C (eds) Cell mechanics. From single scale-based models to multiscale modeling. CRC Press, Boca Raton

Chauviere A, Hillen T, Preziosi L (2007) Modeling cell movement in anisotropic and heterogeneous network tissues. Netw Heterog Media 2:333–357

Chauviere A, Hatzikirou H, Kevrekidis I, Lowengrub J, Cristini V(2012) Dynamic density functional theory of solid tumor growth: preliminary models. AIP Adv 2:011210/1–011210/13

Claes A, Idema A, Wesseling P (2007) Diffuse glioma growth: a guerilla war. Acta Neuropathol 114:443–458

Clatz O, Sermesant M, Bondiau P, Delignette H, Warfield S, Malandain G, Ayache N (2005) Realistic simulation of the 3D growth of brain tumors in MRI images coupling diffusion with biomechanical deformation. IEEE Trans Med Imag 24(10):1334–1346

Cobzas D, Mosayebi P, Murtha A, Jagersand M (2009) Tumour invasion margin on the Riemannian space of brain fibers. In: International Conference on Medical Image Computing and Computer Assisted Intervention, MICCAI

Coons S (1999) Anatomy and growth patterns of diffuse gliomas. In: Berger M, Wilson C (eds) The gliomas. W.B. Saunders Company, Philadelphia, pp 210–225

D'Abaco G, Kaye A (2007) Integrins: molecular determinants of glioma invasion. J Clin Neurosci 14:1041–1048

Daumas-Duport C, Varlet P, Tucker M, Beuvon F, Cervera P, Chodkiewicz J (1997) Oligodendrogliomas. part i: patterns of growth, histological diagnosis, clinical and imaging correlations: a study of 153 cases. J Neuro Oncol 34:37–59

Demuth T, Berens M (2004) Molecular mechanisms of glioma cell invasion and migration. J Neuro Oncol 70:217–228

Descoteaux M (2008) High angular resolution diffusion MRI: from local estimation to segmentation and tractography, Ph.D. thesis, Université Nice-Sophia Antipolis

Descoteaux M, Deriche R, Knische T, Anwander A (2009) Deterministic and probabilistic tractography based on complex fibre orientation distribution. IEEE Trans Med Imag 28(2):269–286

Erban R, Othmer H (2005) From signal transduction to spatial pattern formation in E. coli: a paradigm for multiscale modeling in biology. Multiscale Model Simul 3(2):362–394

Ern A, Stephansen AF, Zunino P (2009) A discontinuous Galerkin method with weighted averages for advection-diffusion equations with locally small and anisotropic diffusivity. IMA J Numer Anal 29(2):235–256

Filbet F, Laurencot P, Perthame B (2005) Derivation of hyperbolic models for chemosensitive movement. J Math Biol 50:189–207

Firmani B, Guerri L, Preziosi L (1999) Tumor immune system competition with medically induced activation disactivation. Math Models Methods Appl Sci 9:491–512

Frieboes H, Jin F, Chuang Y, Wise S, Lowengrub J, Cristini V (2010) Three-dimensional multispecies tumor growth-ii: tumor invasion and angiogenesis. J Theor Biol 264:1254–1278

Geho D, Bandle R, Clair T, Liotta L (2005) Physiological mechanisms of tumor-cell invasion and migration. Physiology 20:194–200

Gerstner E, Chen P-J, Wen P, Jain R, Batchelor T, Sorensen G (2010) Infiltrative patterns of glioblastoma spread detected via diffusion MRI after treatment with cediranib. Neuro Oncol 12(5):466–472

Giese A, Kluwe L, Meissner H, Berens ME, Westphal M (1996) Migration of human glioma cells on myelin. Neurosurgery 38:755–764

Giese A, Westphal M (1996) Glioma invasion in the central nervous system. Neurosurgery 39:235–252

Gritsenko P, Ilina O, Friedl P (2012) Interstitial guidance of cancer invasion. J Pathol 226:185–199

Grünbaum D (2000) Advection-diffusion equations for internal state-mediated random walks. SIAM J Appl Math 61:43–73

Hagman P, Jonasson L, Maeder P, Thiran J-P, Wedeen V, Mueli R (2006) Understanding diffusion MR imaging techniques: from scalar diffusion-weightred imaging to diffusion tensor imaging and beyond. RadioGraphics 26:205–223

Hanahan D, Weinberg R (2011) Hallmarks of cancer: the next generation. Cell 144(5):646–674

Hatzikirou H, Deutsch A (2008) Cellular automata as microscopic models of cell migration in heterogeneous environments. Curr Top Dev Biol 81:401–434

Hillen T (2003) Transport equations with resting phases. Euro J Appl Math 14(5):613–636

Hillen T (2005) On the L^2-moment closure of transport equations: the general case. Discret Contin Dyn Syst Ser B 5(2):299–318

Hillen T (2006) M^5 mesoscopic and macroscopic models for mesenchymal motion. J Math Biol 53:585–616

Hillen T, Othmer H (2000) The diffusion limit of transport equations derived from velocity jump processes. SIAM J Appl Math 61(3):751–775

Hillen T, Painter K (2013) Transport and anisotropic diffusion models for movement in oriented habitats. In: Lewis M, Maini P, Petrovskii S (eds) Dispersal, individual movement and spatial ecology, Vol 2071 of Lecture Notes in Mathematics. Springer, Berlin, p 46

Hood J, Cheresh D (2002) Role of integrins in cell invasion and migration. Nat Rev Cancer 2:91–100

Huttenlocher A, Horwitz A (2011) Integrins in cell migration. Cold Spring Harb Perspect Biol 3:1–16

Jbabdi A, Mandonnet E, Duffau H, Capelle L, Swanson K, Pelegrini-Issac M, Guillevin R, Benali H (2005) Simulation of anisotropic growth of low-grade gliomas using diffusion tensor imaging. Mang Res Med 54:616–624

Kelkel J, Surulescu C (2011) On some models for cancer cell migration through tissue networks. Math Biosci Eng 8(2):575–589

Kelkel J, Surulescu C (2012) A multiscale approach to cell migration in tissue networks. Math Models Methods Appl Sci 23(3):1150017/1–1150017/25

Konukoglu E, Clatz O, Bondiau P, Delignette H, Ayache N (2010) Extrapolation glioma invasion margin in brain magnetic resonance images: suggesting new irradiation margins. Med Image Anal 14:111–125

Lauffenburger D, Lindermann J (1993) Receptors. Models for binding, trafficing and signaling. Oxford University Press, Oxford
LeBihan D, Mangin J, Poupon C, Clark C, Pappata S, Chabriat H (2001) Diffusion tensor imaging:concepts and applications. J Magn Reson Imag 13:534–546
Lorenz T, Surulescu C (2014) On a class of multiscale cancer cell migration models: well-posedness in less regular function spaces. Math Models Method Appl Sci 24:2383–2436
Maini P (1989) Spatial and spatio-temporal patterns in a cell-haptotaxis model. J Math Biol 27:507–522
Mardia K, Jupp P (1999) Direct Stat. Wiley, New York
Matiello J, LeBihan D (1994a) Estimation of the effective self-diffusion tensor from the NMR spin echo. J Magn Reson 103:247–254
Matiello J, LeBihan D (1994b) Mr diffusion tensor spectroscopy and imaging. Biophys J 66(1):259–267
Matsukado Y, MacCarty C, Kernohan Jea (1961) The growth of glioblastoma multiforme (astrocytomas, grades 3 and 4) in neurosurgical practice. J Neurosurg 18:636–644
Meral G, Stinner C, Surulescu C (2013) On a multiscale model involving cell contractivity and its effects on tumor invasion. Preprint, TU Kaiserslautern, Submitted
Meral G, Surulescu C (2013) Mathematical modelling, analysis and numerical simulations for the influence of the heat shock proteins on tumour invasion. J Math Anal Appl 408:597–614
Mosayebi P, Cobzas D, Jagersand M, Murtha A (2010) Stability effects of finite difference methods on a mathematical tumor growth model. In: Computer vision and pattern recognition workshops (CVPRW), 2010 IEEE Computer Society Conference, IEEE Conference Proceedings, pp 125–132
Moschos S, Drogowski L, Reppert S, Kirkwood J (2007) Integrins and cancer. Oncology 21(9):13–20
Ohgaki H, Kleihues P (2005) Epidemiology end etiology of gliomas. Acta Neuropathol 109:93–108
Othmer H, Dunbar S, Alt W (1988) Models of dispersal in biological systems. J Math Biol 26:263–298
Othmer H, Hillen T (2002) The diffusion limit of transport equations ii: Chemotaxis equations. SIAM J Appl Math 62:1222–1250
Painter K, Hillen T (2013) Mathematical modelling of glioma growth: the use of diffusion tensor imaging (DTI) data to predict the anisotropic pathways of cancer invasion. J Theor Biol 323:25–39
Sidani M, Wessels D, Mouneimne G, Ghosh M, Goswami S, Sarmiento C, Wang W, Kuhl S, El-Sibai M, Backer J, Eddy R, Soll D, Condeelis J (2007) Cofilin determines the migration behavior and turning frequency of metastatic cancer cells. J Cell Biol 179(4):777–791
Stinner C, Surulescu C, Winkler M (2013) Global weak solutions in a PDE-ODE system modeling multiscale cancer cell invasion. Preprint, TU Kaiserslautern. submitted
Stolarska M, Kim Y, Othmer H (2009) Multiscale models of cell and tissue dynamics. Philos Trans R Soc A 367:3525–3553
Stroock D (1974) Some stochastic processes which arise from a model of the motion of a bacterium. Zeitschrift für Wahrscheinlichkeitstheorie und verwandte Gebiete 28:305–315
Sun S, Titushkin I, Cho M (2006) Regulation of mesenchymal stem cell adhesion and orientation in 3d collagen scaffold by electrical stimulus. Bioelectrochemistry 69:133–141
Sundgren P, Dong Q, Gomez-Hassan D, Mukherji S, Maly P, Welsh R (2004) Diffusion tensor imaging of the brain: review of clinical applications. Neurocarciology 46:339–350
Surulescu C, Surulescu N (2010) A nonparametric approach to cell dispersal. Int J Biomath Biostat 1:109–128
Surulescu C, Surulescu N (2011) Modeling and simulation of bacterial motion via a nonparametric method. Math Biosci Eng 8:263–277
Surulescu C, Surulescu N (2013) Some classes of stochastic differential equations as an alternative modeling approach to biomedical problems. In Kloeden PE, Pötzche C (eds) Random and nonautonomous dynamical systems in the life sciences. LNM Biomathematics Series 2102, pp 269–307
Szymanska Z, Urbanski J, Marciniak-Czochra A (2009) Mathematical modelling of the influence of heat shock proteins on cancer invasion of tissue. J Math Biol 58:819–844
Tanaka M, Debinski W, Puri I (2009) Hybrid mathematical model of glioma progression. Cell Prolif 42:637–646
Tosin A, Preziosi L (2010) Multiphase modeling of tumor growth with matrix remodeling and fibrosis. Math Comput Model 52:969–976
Traqui P (1995) From passive diffusion to active cellular migration in mathematical models of tumour invasion. Acta Biotheor 43:443–464
Tuch D (1996) Diffusion MRI of complex Tissue Structure, Ph.D. thesis, University of Chicago
Tuch D (2004) Q-ball imaging. Magn Reson Med 52(6):1358–1372

Wheeler MF (1978) An elliptic collocation-finite element method with interior penalties. SIAM J Numer Anal 15(1):152–161
Wrensch M, Minn Y, Chew T, Bondy M, Berger M (2002) Epidemiology of primary brain tumors: current concepts and review of the literature. Neuro Oncol 4(4):278–299
Xue C, Othmer H (2009) Multiscale models of taxis-driven patterning in bacterial populations SIAM Journal for. Appl Math 70(1):133–167